UL- ACX8153 FMT A RT z DT 08/12/92 R/DT 08/12/92 STAT mm E/L n
SRC c LANG ??? ROM n MOD    UNIQUE n GOVT ? S/SYS n D/I n SUBD n NUM a S/TYP a
NAME a SUBJ a SER a KIND a H/ESTAB a T/EVAL a IP a RULES c

010: :: :a n 86703422
040: :: :a DGPO/DLC :c DLC :d DLC
130: 0: :a Research and development technical report (United States. Army
Electronics Command)
410/1:10: :a United States. :b Army Electronics Command. :t Research and
development technical report
430/2: 0: :a R & D technical report (United States. Army Electronics Command)
430/3: 0: :a ECOM (Series) (United States. Army Electronics Command)
430/4: 0: :w nnaa :a Research and development technical report
430/5: 0: :a Technical report (United States. Army Electronics Command)
643/1: :: :a Fort Monmouth, N.J. :b U.S. Army Electronics Command
644/1: :: :a f (fully analyzed) :5 All locations
645/1: :: :a n (not traced) :5 All locations
646/1: :: :a s (classed sep) :5 All locations
667/1: :: :a Document.
670/1: :: :a Supt. of Docs. no.: D 111.9/4:5830.

690/1: :: :a sc4 8/10/92

099 UMR1069

100 Carpenter, John F. G. (John F.)

245 / 260 4c 1963 / 300 IX, 95 p. : ib. ill. ; 4c 28 cm.

533 Photocopy. #b Ann Arbor, Mich. #6 Unnersity
Microfilms, Inc.), 4d 1967. 4e 21 cm.

Nuclear spectroscopy.

656-0 Nuclear spectroscopy.

656-0 " Iowa.

650-0 Interferometer, Michelson.
Gamma ray spectrometer.
Thesis (Ph. D.) — Univ of Mich., 1963.

Michelson spectroscopic
Iowa.

502 Thesis (Ph. D.) — Univ. of Mich.

710 20 Univ of Mich.

CARPENTER, John Marland, 1935–
  PREDICTION AND MEASUREMENT OF NEUTRON
  CHOPPER BURST SHAPES.

The University of Michigan, Ph.D., 1963
Engineering, nuclear

*enzym*
UMR 1069

# PREDICTION AND MEASUREMENT OF NEUTRON CHOPPER BURST SHAPES

by

John Marland Carpenter

Applying an original method* for the graphic representation
of the angular and spatial density of neutrons in a collimated
beam, a technique is developed for calculation of the number c.
neutrons passed through one or more rotating elements in such
a beam.  The P-gram construction is briefly discussed.  The effects
of moving elements in a beam of finite-velocity neutrons are described.
The apparent configuration of the rotating element is shown to
differ from that of a stationary element and the apparent collimator
formed by it is represented in terms of the P-gram construction.
Consideration of the joint probability of transmission of a neutron
through both a stationary collimator which defines a beam, and
through a rotor, which interrupts the beam, leads to an expression
for the time-dependent neutron transmission probability.

An experiment is described in which a monochromatic neutron
beam was selected by means of a crystal monochromator and the
method is applied to its analysis.  Formulae are presented which
can be used for hand calculation of results to be expected in
the experiment.  Results of the measurements are displayed and
these demonstrate the validity of the calculations.

---

*Carpenter, John M.; "A Construction for the Investigation
of Collimator Performance," work unpublished.  The method of this
paper will be referred to as the "P-gram construction."

PREDICTION AND MEASUREMENT OF NEUTRON
CHOPPER BURST SHAPES

by

John Marland Carpenter

A dissertation submitted in partial fulfillment
of the requirements for the degree of
Doctor of Philosophy in The
University of Michigan
1963

Doctoral Committee:

    Associate Professor Dietrich H. Vincent, Chairman
    Professor Albert E. Heins
    Professor William Kerr
    Professor John S. King
    Professor Paul F. Zweifel

TABLE OF CONTENTS

TABLE OF CONTENTS (Concluded)

# LIST OF FIGURES

iv

## LIST OF TABLES

# ACKNOWLEDGEMENT

CHAPTER I

INTRODUCTION AND DESCRIPTION OF THE PROBLEM

The development of nuclear reactors and other devices
as plentiful sources of neutrons led to experiments involved
with determining the energy spectra of neutrons. In addi-
tion to spectral examinations of the sources themselves,
these experiments include use of the neutrons as a probing
radiation for studies of properties of nuclei and systems
of nuclei. This is in just the same sense as that in which
sources of electromagnetic and acoustical, and also other
particle radiations have been studied and used as probes.
A branch of spectroscopy has developed with the use of each
of these radiations in this way, and sub-branches according
to wavelength or energy. Each is supplied with its own kit
of tools, and each has been found useful for studying cer-
tain classes of problems.

One of the tools in each branch of spectroscopy is a
device for analyzing spectra according to energy (velocity,
frequency or wavelength.) In neutron spectroscopy one of
the basic tools is a mechanical shutter. This is a device
by means of which a beam of neutrons is opened for a short
interval of time, then closed, producing a short burst of
neutrons. The neutrons in the beam, having a distribution
of velocities, will arrive at a point some distance down-
stream at different times according to their velocities.
If one detects and sorts out these neutrons according to the

time of their arrival, then this sorting according to times
of flight is a velocity analysis. Figure 1 shows schemati-
cally a time-of-flight spectrometer, and 2 a plot of neutron
intensity as a function of time at several downstream points
from the shutter. Velocity analysis by this method is not
new, nor is it confined to neutron, nor even to particle
analyzers. Fermi, Marshall, and Marshall[1] operated the
first such neutron "chopper" system in 1943.

Erected at the University of Michigan Ford Nuclear
Reactor is a spectrometer which operates upon this same
principle.* It is intended, however, for investigation of
neutron scattering events, and the change of speed and direc-
tion experienced by the neutron in the scattering inter-
action. Thus in this device the velocity analysis is done
twice, once before scattering, again after scattering. Fig-
ure 3 shows the University of Michigan machine diagrammati-
cally. Two shutters perform the analysis of neutrons incident
on the scatterer. The first produces a short burst contain-
ing neutrons of many speeds which travel a distance L and
then are incident on the second shutter. The neutrons arrive
at the second shutter at different times according to their
speeds. If one briefly opens the second shutter at some

(1) Fermi, E.; Marshall, J.; and Marshall, L.; Phys. Rev. 72,
p. 193, (1947)

*The University of Michigan device in many respects is pat-
terned after that of Egelstaff and co-workers at Chalk River,
for example, see Egelstaff, P. A.; Cocking, S. J.; and
Alexander, T. K.; IAEA Proc. of the Symposium on Inelastic
Scattering of Neutrons in Solids & Liquids, Vienna, Oct., 1960,
p. 165, IAEA (1961). We shall refer to this paper as reference 6.
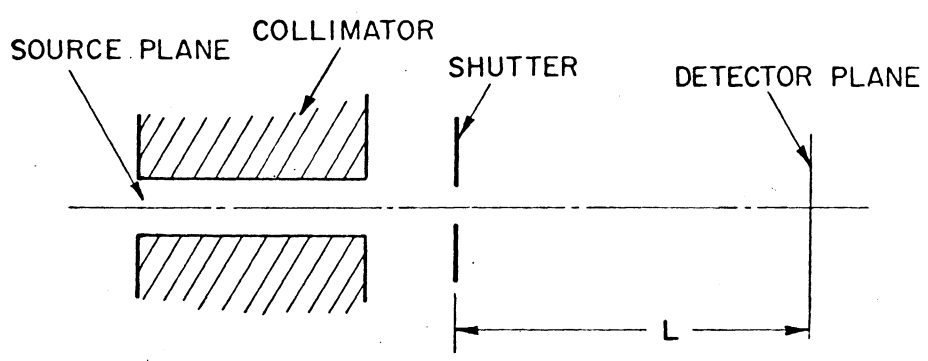
Figure 1. A schematic representation of a simple chopper system.
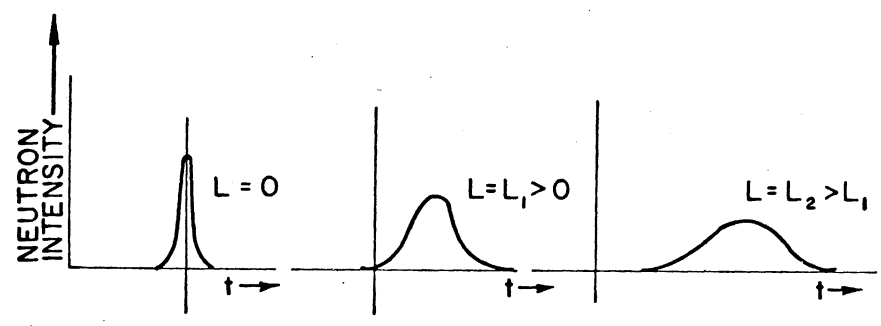


Figure 2. The Neutron intensity as a function of time at three successive points in a chopped neutron beam containing neutrons of many velocities.
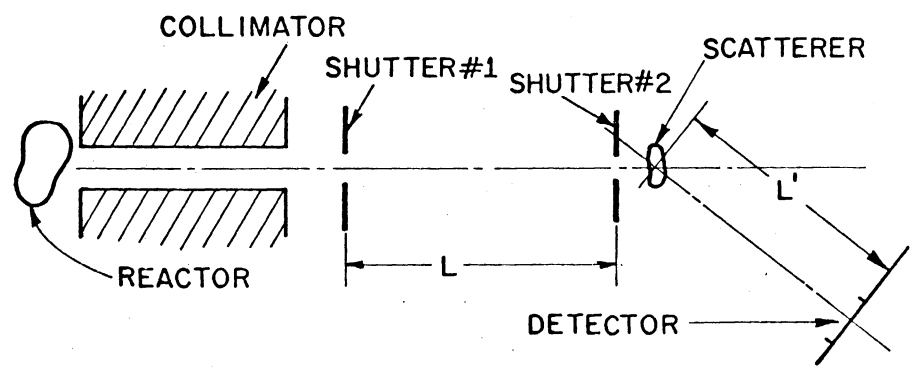


Figure 3. A schematic representation of a mechanical neutron monochromator used in a scattering experiment.

time t  later, a burst of neutrons of well-determined speed
$v = \frac{L}{t}$ will pass,  The neutrons then strike the scatterer and
in general, change their speeds.  The second velocity analy-
sis is done by time of flight, that is, the neutrons are
allowed to travel a distance  L' after scattering, and are
then detected.  A neutron detected at time  t'  after the
burst strikes the scatterer, thus had a final speed $v' = \frac{L'}{t'}$.

In the University of Michigan machine, the shutters are
rotating discs with several parallel, curved slits across
the diameter; as the slits pass parallel to the beam of neu-
trons, neutrons pass through in a short burst.  The duration
of the burst, and also the number of neutrons in the burst,
is determined by the size and angular divergence of the
beam, and by the angular velocity and slit configuration
of the rotor.  It is the purpose of this paper to develop a
method for predicting as a function of time the number of
neutrons passed by a system of rotors of this kind.  Other
notable efforts to this end have been made by Stone and
Slovacek[2] and Marseguerra and Pauli[3]:  The work of these
authors was directed toward prediction of the performance of
single-rotor systems and is not readily generalized to multi-
rotor systems.  Also, these authors treated somewhat idealized,
albeit useful, models of chopper systems; Marseguerra and
Pauli a uniform, unidirectional beam, and Stone and Slovacek

(2) Stone, R. S.; and Slovacek, R.E.; KAPL 1499 (1956)
(3) Marseguerra, M.; and Pauli, G.; Nuclear Instruments and
Methods 4, pp. 140-150, (1959)

a beam distributed uniformly in angle and uniformly in space.
The method of this paper may be used to calculate the per-
formance of a multi-rotor system, and properly accounts for
the spatial and angular distribution of the beam passed
through the system.  It is based upon the author's "P-gram"
construction[4], which was developed to investigate the
angular and spatial distribution of a beam defined by an
arbitrary collimating system of rectangular geometry.

---

(4)  Carpenter, J. M.; work unpublished

# CHAPTER II

## USE OF THE P-GRAM* CONSTRUCTION
## FOR THE CALCULATION OF CHOPPER BURST SHAPES

A. Introduction of the P-gram Construction

Let us begin by discussing briefly the idea behind the

P-gram construction. We shall speak in the context of the

following diagrams, figure 4 and figure 5.

The neutron trajectory, in direction $\Omega$ is specified in

terms of angles $\varphi$ and $\psi$. The angle $\varphi$ is the angle between

the x - axis and the projection of $\Omega$ against the x-y plane,

while $\psi$ is correspondingly measured in the x-z plane.

These are not the angles of the usual polar coordinate repre-

sentation but are appropriate here because most collimating

elements are Soller Slits, that is, they have rectangular

cross sections. In this case the probability that a neutron

which crosses a downstream point x, y, z in direction $\varphi$, $\psi$

be transmitted through the collimating system is separable

into the product of two factors. One is dependent upon x,

y, $\varphi$ and the other is dependent upon x, z, $\psi$. Here we have

assumed y and z to be measured along the rectangular

cross-sections of the collimator(s) while x is measured

as the distance downstream from some reference point. The

probabilities dependent upon x, y, $\varphi$ can thus be considered

independently of those for x, z, $\psi$.

This separation is the more significant because in

---

*See footnote below
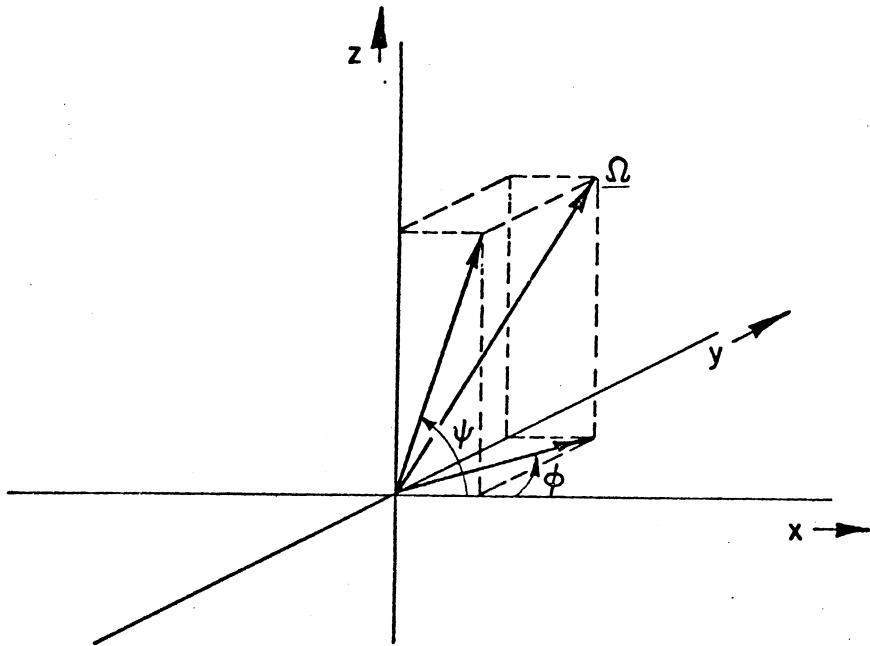
Figure 4. The coordinate system in terms of which collimator transmission probabilities are separable for Soller Slit collimators. The x-direction is the direction of the collimator centerline. The y-direction is taken parallel to the vertical dimension of the rectangular collimator aperture. The z-direction is parallel to the horizontal dimension.



COLLIMATOR 1          COLLIMATOR 2
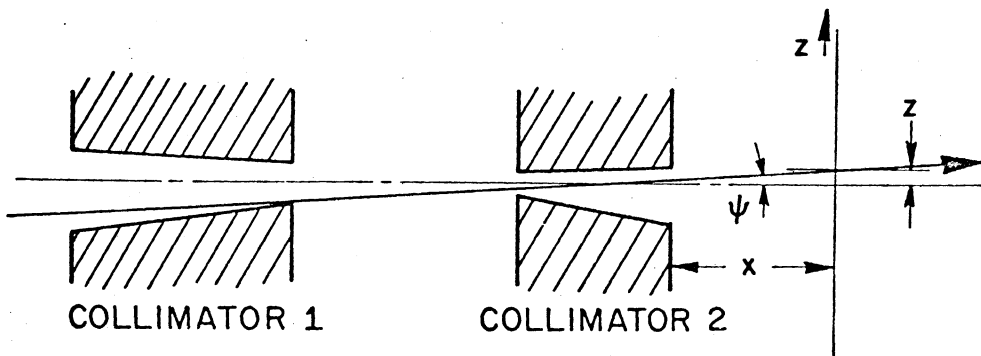
Figure 5. A section through two successive collimators in the resolution plane, showing a transmitted neutron trajectery and its intercept on a screen at position x.

most cases only one plane is important for calculating chopper
resolution. The rotor turns in this plane. We chose it to
be the x, z plane and consider angles $\psi$ in this plane.
Having restricted our attention to effects in the "resolution"
plane, we erect an imaginary screen at an arbitrary down-
stream point x, and at that point draw z, $\psi$ axes as in
figure 6.

Each point on the z, $\psi$ plane specifies a trajectory.
The collimator will allow neutrons to cross the screen at
x for some trajectories z, $\psi$ and will not allow those
others for which the trajectory passes through the walls of
the collimator. We draw a diagram in the z, $\psi$ plane, the
interior of which corresponds to "allowed" trajectories for
which the transmission probability is unity. The exterior
corresponds to those trajectories which intersect collimator
boundaries and for these, the transmission probability is
zero. We call this diagram a P-gram.* We define a function
$P(x,z,\psi)$ which is unity inside the P-gram, zero outside,
i.e., P = 1 if z, $\psi$ satisfy certain conditions, and P = 0
otherwise. The function P is the transmission probability.

The function P depends upon the downstream distance,
x, at which the beam is examined, to the extent that this
distance establishes the shape of the P-gram. We shall carry

---

*The word "P-gram" is used here to designate the region in
the z, $\psi$ plane containing transmitted trajectories. For
simple collimators, this region has the shape of a parallelo-
gram, while it also represents the region of unit trans-
mission probability, thus the name "P-gram."
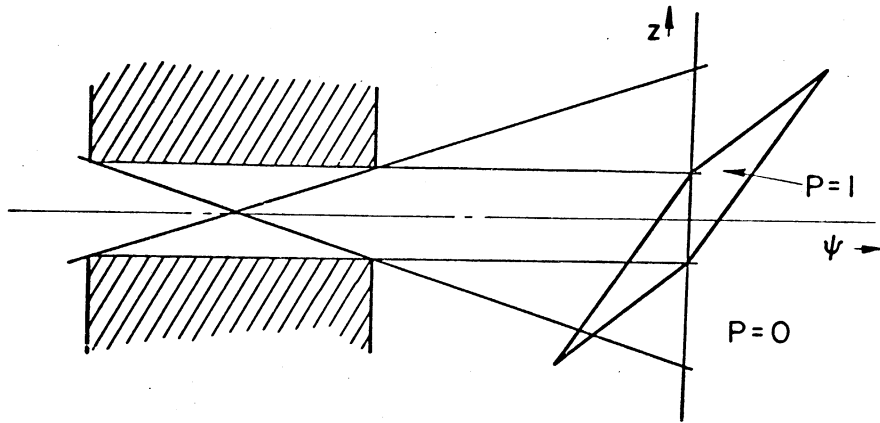
**Figure 6.** Section through a collimator and the trajectory plane (z-$\psi$) plane showing the region of transmitted trajectories (P-gram).

x as an argument in P therefore to indicate this fact.
In those instances where formulae are presented, the origin
of that coordinate will be specified.

The utility of the construction is further enhanced if
one notes that if there is more than one collimator in the
beam, then the event of tranmission through all consists of
transmission through each individually. Thus the probability
of transmission through all is the product of probabilities
for transmission through each, since these are independent
events. The P-gram picture then consists of several over-
lapping P-grams, each appropriate to one collimating element,
and the overlapping areas are those in which the joint trans-
mission probability is unity. Thus if $P_1(x,z,\psi)$ is the pro-
bability of transmission of neutron x, z, $\psi$ through colli-
mator 1 and $P_2(x,z,\psi)$ is for collimator 2, then $P_{12}(x,z,\psi)$,
the probability of transmission through both is

$$P_{12}(x,z,\psi) = P_1(x,z,\psi)\ P_2(x,z,\psi).$$

(II-1)

B. The P-gram for a Chopper Rotor

The rotating slits of a chopper rotor may be considered
to constitute a collimator. There is the added complication
that the orientation of the rotor is not constant with time.
However, consider carefully the following argument for a
stationary collimator oriented with its slit centerline at
some angle $\theta$ with respect to the beam centerline (x - axis)
as in figure 7. The slit centerline projects to a point

$x\theta$ on the z - axis; the maximum angle transmitted is $\theta + \psi_{max.}$; the minimum is $\theta + \psi_{min.}$. A P-gram for this slit may be drawn but it is centered about $z = x\theta$, and $\psi = \theta$. For small angles the P-gram for this slit is the same when the slit is oriented off-axis by an angle $\theta$ as when it is oriented with the beam axis, except for this displacement. If this angle $\theta$ is time dependent, $\theta = \omega t$, the rotor P-gram moves in the z, $\psi$ plane with its center along the locus $z = x\omega t$, $\psi = \omega t$ (or $z = x\psi$) as in figure 8. For counterclockwise rotation, as assumed, motion is in the direction of the arrow; if rotation is clockwise, then the rotor P-gram moves in the opposite direction.

The P-grams of figures 7 and 8 represent regions of allowed trajectories for neutrons of infinite speed, which cross the rotor centerplane when the rotor is oriented at angle $\theta = \omega t$. For neutrons of finite speed the slit will appear curved, and the P-grams will have a different shape. We reserve until later the problem of calculating this effect. For now, let us address the problem of assigning some meaning to the P-gram as seen in a coordinate system moving along with it as it traverses the z, $\psi$ plane.

Recall that the time reference $t = 0$ is the time at which the slit centerline is parallel to the beam axis. At any later time t the slit centerline will be oriented at an angle $\omega t$ from the beam axis. The region of allowed trajectories (P-gram) for neutrons which cross the rotor centerplane when its slit is parallel to the beam axis is

- 12 -
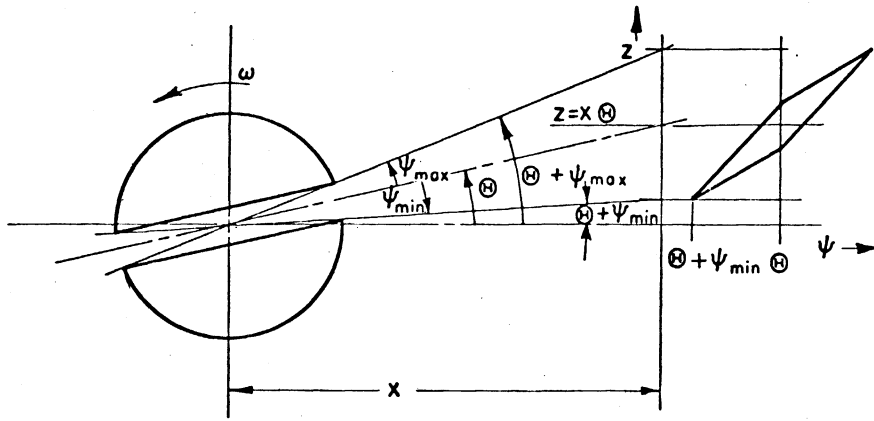


**Figure 7.** Section through a rotor turned at angle $\theta$ from the reference axis, showing the region of transmitted trajectories on a trajectory plane at distance x from the rotor centerplane
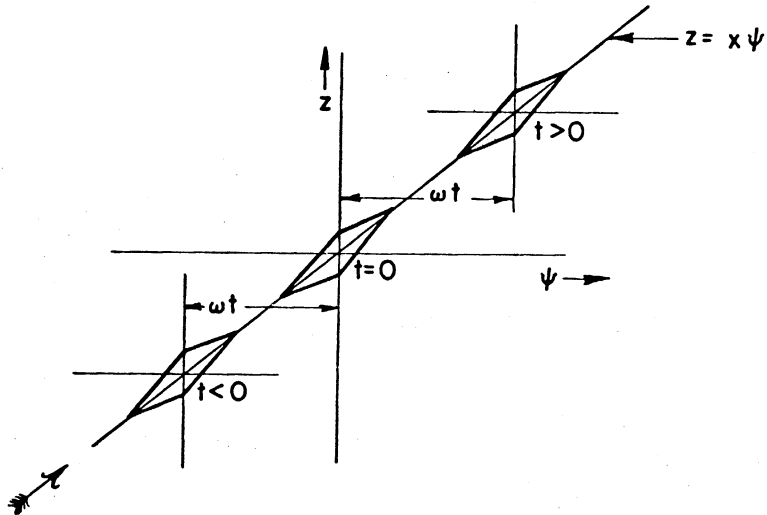


**Figure 8.** Positions of the P-gram for a spinning rotor at several times.

centered at $z = 0$, $\psi = 0$. The P-gram for neutrons which
cross the rotor centerplane when its slit is at angle $\omega t$ to
the beam axis, is centered at $z = x\omega t$, $\psi = \omega t$. This is to
say, the P-gram displaced to the point $z = x\omega t$, $\psi = \omega t$ is
for neutrons which cross the rotor centerplane at time $t$.
The P-gram retains its shape for each time $t$ (angle $\omega t$).

Thus we need only consider the shape of the P-gram
for neutrons which cross the rotor centerplane at time zero,
at which time the slit centerline is parallel to the x axis.
The shape will depend upon the physical configuration of the
rotor, the neutron speed and the rotor angular speed. We
shall work here with a straight slit rotor, but we will
later show that the results thus derived are applicable to
the entire class of curved slit rotors with Archimedes'
Spiral centerlines, or those which approximate this condi-
tion. The equations for the apparent slit boundaries des-
cribe the walls of a collimator which we may now consider
to be stationary. From these the boundaries of a P-gram
may be determined.

C. Apparent Slit Boundaries

Let us derive the equations for the apparent slit
boundaries as seen by a neutron crossing the rotor center-
plane at time zero. Refer to figure 9, where symbols used
here are defined. In a coordinate system fixed in the rotor
$(x',z')$ the straight slit boundaries are given by $z' = \pm h/2$
(choose + for upper, - for lower boundary). Here, $h$ is the
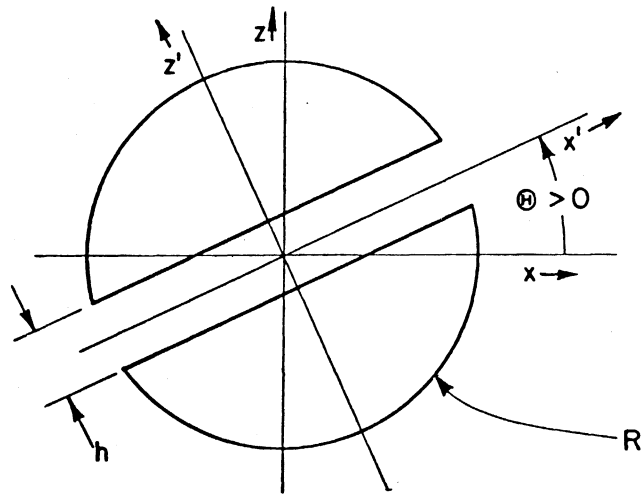
Figure 9. Coordinate systems (x,z) fixed in space and (x',z') fixed in a rotor turned at angle $\theta$, and the boundaries of a straight-slit rotor.
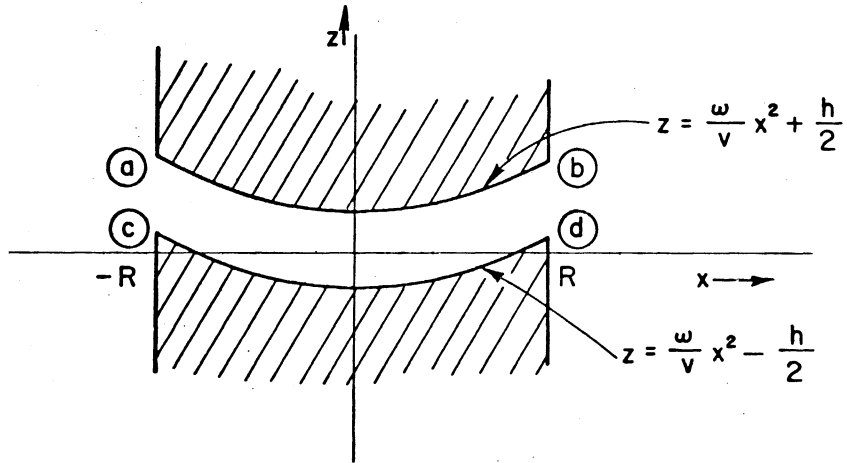


Figure 10. The apparent collimator boundaries of a straight-slit rotor turning at angular velocity $\omega$, as seen by a neutron of speed v.

width of the rotor slit.

Coordinates in the x', z' system are given in terms of those in the x, z, system through the transformation

$$
\begin{cases}
x' = x \cos \theta + z \sin \theta \\
z' = -x \sin \theta + z \cos \theta
\end{cases}
\tag{II-2}
$$

Thus in terms of the coordinates of the stationary system, the boundaries are given by

$$
\pm h/2 = -x \sin \theta + z \cos \theta \tag{II-3}
$$

For a spinning rotor, $\theta = \omega t$, so that at any instant $t$ the slit boundaries are

$$
\pm h/2 = -x \sin \omega t + z \cos \omega t \tag{II-4}
$$

The apparent slit boundaries are given by the intersections of a neutron plane wave moving at some speed $v$, and crossing the rotor centerplane $x = 0$ at $t = 0$, which is represented by the line

$$
x = vt \tag{II-5}
$$

The apparent boundaries are thus parametrically

$$
\begin{cases}
x = vt \\
-x \sin \omega t + z \cos \omega t = \pm h/2
\end{cases}
\tag{II-6}
$$

The parameter $t$ may be eliminated rigorously but it is adequate for our purposes to restrict our attention to small times ($\omega t \ll 1$) which correspond to small angles; then we have

$$
\begin{cases}
x = vt \\
-x\omega t + z = \pm h/2
\end{cases}
\tag{II-7}
$$

and eliminating parameter t,

$$- \frac{\omega}{v} x^2 + z = \pm h/2;$$

$$z_{\pm} = \frac{\omega}{v} x^2 \pm \frac{h}{2} \qquad \text{(II-8)}$$

These equations (+ for upper, and - for lower) represent the apparent boundaries of a slit rotating at angular speed $\omega$, as seen by a neutron moving at speed $v$.* They pertain of course only for $-R \leq x \leq R$, and are derived for neutrons crossing the rotor centerplane at $t = 0$, when the slit is parallel to the beam axis. The boundaries are parabolic, and are symmetric functions of $x$. Moreover note that the boundary equations are dependent only upon the ratio $\frac{\omega}{v}$, and that for $v \rightarrow \infty$ or $\omega = 0$ the equations are those of a straight slit, $z = \pm h/2$.

D. The P-gram for the Apparent Boundaries of a Rotating Slit

On figure 10 is drawn the collimator formed by the apparent slit boundaries for finite $v$. We wish to derive a P-gram for this collimator. For this purpose we may note that the re-entrant surface (lower boundary on figure 10) is not effective as a collimating surface, and it is the edges (c) and (d) which are important. The upper surface establishes a limiting condition on trajectories $z$, $\psi$, which are tangent to it for $-R \leq x \leq R$, and the edges (a) and (b) may also

*These results correspond to those of Marseguerra and Pauli, who used the notation $y_u^*$ (x) and $y_L^*$ (x) for our $z_+$ (x) and $z_-$ (x).

limit the trajectories.

The P-gram boundaries on a screen at a distance L from the rotor axis are established by several conditions. For trajectories z, $\psi$ which just touch an edge, say (c), there is a unique relation between z and $\psi$ which gives the P-gram boundary, see figure 11. The value of z on the screen at L is shown for a trajectory with angle $\psi$, which grazes the edge (c). The relation thus established between z and $\psi$ is the boundary of the rotor P-gram due to edge (c). For each edge therefore we have the boundary equations:

Edge (a):  $z = h/2 + \frac{\omega}{v} R^2 + (L + R) \psi$          (II-9a)

Edge (b):  $z = h/2 + \frac{\omega}{v} R^2 + (L - R) \psi$          (II-9b)

Edge (c):  $z = -h/2 + \frac{\omega}{v} R^2 + (L + R) \psi$          (II-9c)

Edge (d):  $z = -h/2 + \frac{\omega}{v} R^2 + (L - R) \psi$          (II-9d)

which are referred to as lines (a), (b), (c), and (d) respectively on figures 12 and 13, which are drawn for the simplifying case L = 0.

In addition to these boundaries due to the edges of the slit, the upper and lower surfaces may bound the rotor P-gram. The limiting trajectory $\psi$ is one which is tangent to the slit surface (say the upper surface) at some point x*, z*. At the tangent point,

$$\psi = \frac{dz}{dx}\bigg|_{x=x^*} = \frac{2\omega}{v} x^*$$
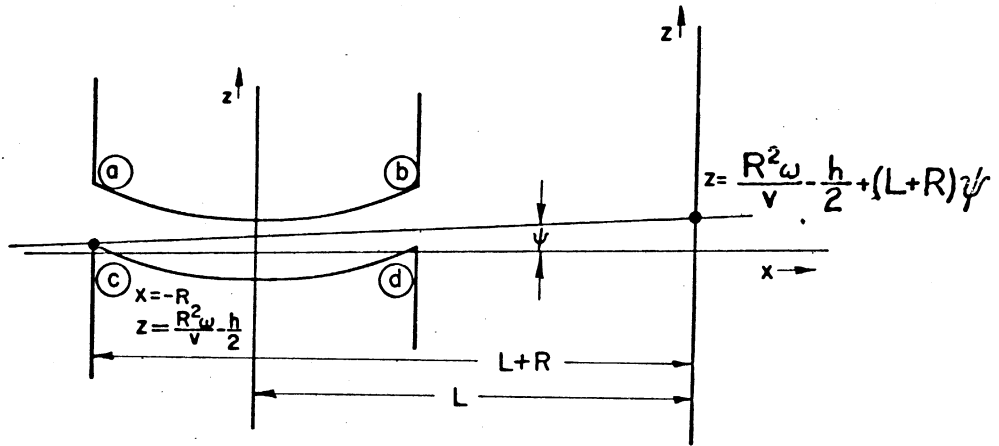
Figure 11. The apparent collimator boundaries for a spinning rotor, and the construction by means of which the corresponding P-gram boundaries are calculated for a screen at distance L from the rotor centerplane.
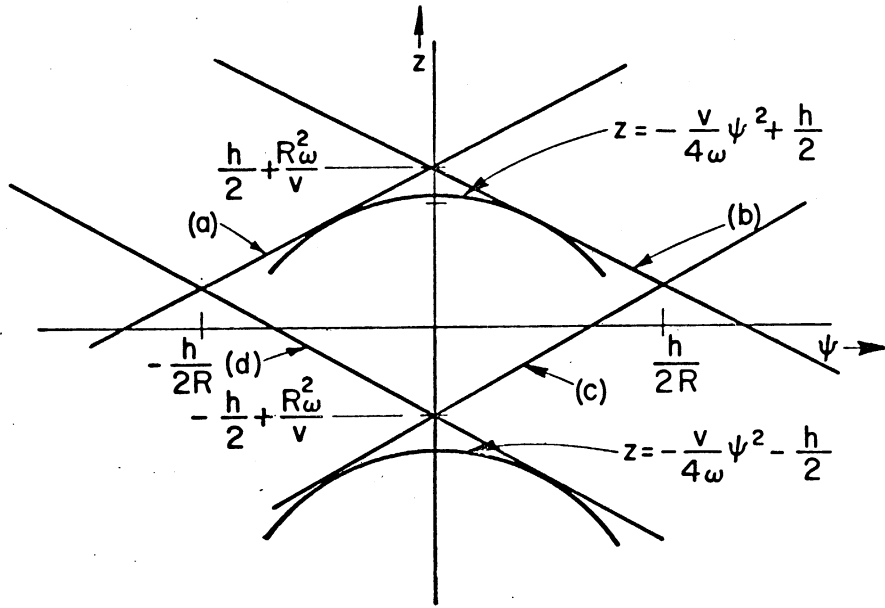
Figure 12. The P-gram for a straight-slit rotor for the condition $v \geqslant 4R^2\omega/h$, $\omega$ counterclockwise.
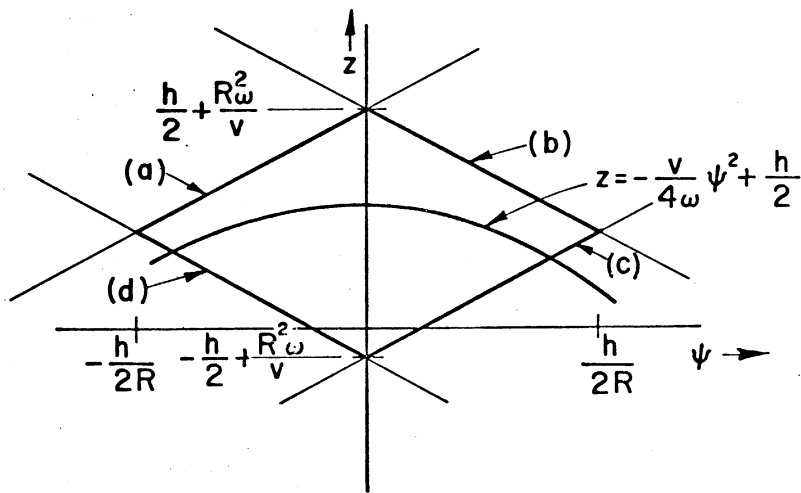


Figure 13. The P-gram for a straight-slit rotor for the condition $R^2\omega/h \leqslant v \leqslant 4R^2\omega/h$, $\omega$ counterclockwise.

from which

$$x^* = \frac{v}{2\omega}\ \psi \qquad\qquad\qquad (II-10)$$

and

$$z^* = \frac{\omega}{v}\ x^{*2} + \frac{h}{2} = \frac{v}{4\omega}\ \psi^2 + \frac{h}{2} \qquad (II-11)$$

On the screen at  L  the value of  z  for this trajectory is

$$z = z^* + (L - x^*)\ \psi$$

$$= \frac{v}{4\omega}\ \psi^2 + \frac{h}{2} + L\ \psi - \frac{v}{2\omega}\ \psi^2$$

$$= -\frac{v}{4\omega}\ \psi^2 + L\ \psi + \frac{h}{2} \qquad\qquad (II-12)$$

In further work, we shall uniformly assume that the screen
is erected at the rotor centerplane, i.e.,  L = 0.

The boundary due to the upper surface intersects the line
(b) at the intersection

$$\begin{cases} z = +\ h/2 + \dfrac{\omega}{v}\ R^2 - R\ \psi \\[2mm] z = -\ \dfrac{v}{4\omega}\ \psi^2 + h/2 \end{cases} \qquad (II-13)$$

from which

$$\frac{v}{4\omega}\ \psi^2 - R\ \psi + \frac{\omega}{v}\ R^2 = 0$$

$$\psi = \frac{4\omega}{v}\ (x)\ \frac{R \overset{+}{-} \sqrt{R^2 - 4\ \dfrac{v}{4\omega}\ \dfrac{\omega}{v}\ R^2}}{2}$$

$$= 2\ R\ \omega/v \qquad\qquad\qquad (II-14)$$

For $\frac{\omega}{v}$  such that this intersection coincides with the inter-
section of (b) and (c), lines (a) and (b) no longer bound the

P-gram. The P-gram of figure 12 thus is for the condition

$$\frac{2R\omega}{v} \leqslant \frac{h}{2R}$$

or

$$v \geqslant \frac{4R^2\omega}{h} \qquad\qquad (II\text{-}15)$$

For the condition

$$v \leqslant \frac{4R^2\omega}{h} \qquad\qquad (II\text{-}16)$$

the picture appears as in figure 13 . From this last diagram we can see that the P-gram completely closes when the intersection of the lines (c) and (d) meets the parabola, i.e., when

$$- h/2 + R^2 \,\omega/v = + h/2$$

$$v = R^2 \,\omega/h \qquad\qquad (II\text{-}17)$$

No neutrons are transmitted when $v \leqslant R^2 \,\omega/h$.

E. The Burst Shape Function, Definition and Derivation of an Expression

We now complete the description of the method of this paper. To this point, we have developed all the results needed to proceed to the calculation of the burst shape. The first is the product rule, equation (II-1).

$$P_{12}(x,z,\psi) = P_1(x,z,\psi)\; P_2(x,z,\psi) \qquad\qquad (II\text{-}1)$$

Using this, we shall say that $P_1(x,z,\psi)$ is the probability of transmission through the collimator of figure 14, and rename it $P_C$. $P_2$ applies to the rotor and we rename it $P_R$.
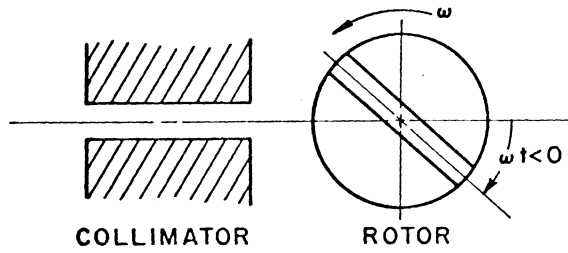
Figure 14. Section through a collimator and a rotor in the resolution plane, showing the rotor turned at a negative angle.
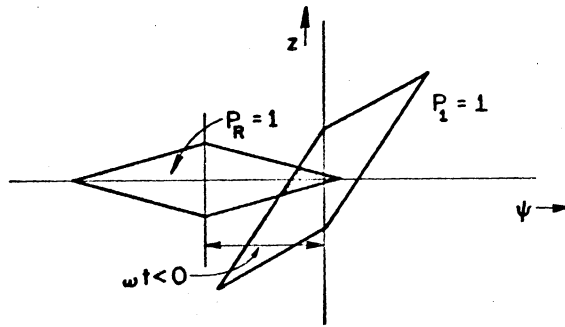


Figure 15. The P-gram picture of the formation of a burst by the rotor-collimator system, for a negative time t. The shaded area is proportional to the number of neutrons transmitted at time t.
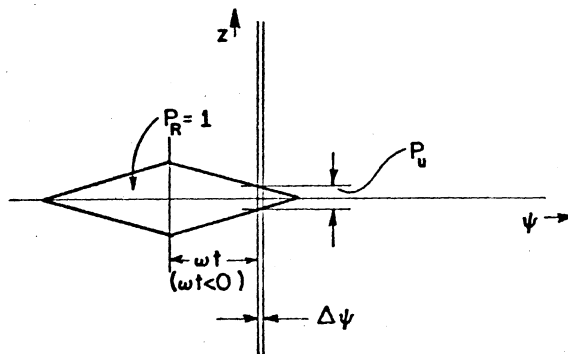


Figure 16. The P-gram picture of the formation of a burst by a rotor in a unidirectional beam.

$P_R$ is a function not only of x, z, $\psi$; but also of the time t and the neutron speed v, rotor speed $\omega$, and rotor parameters. Thus the probability $P(x,z,\psi,v,\omega,t)$ may be written

$$P(x,z,\psi, v,\omega,t) = P_C(x,z,\psi) \, P_R(x,z,\psi,v,\omega,t).$$

$$(II-18)$$

Second we appeal to the assertion of section B which stated that time dependence of the rotor transmission probability is simply described as translation of the P-gram in the z - $\psi$ plane, as a function of t, the shape being unaffected. This may be indicated mathematically by the statement

$$P_R(x,z,\psi,v,\omega,t) = P_R(x,z - L\omega t, \psi - \omega t, v, \omega)$$

$$(II-19)$$

where for $P_R(x,z,\psi,v,\omega)$ we take the function derived in section D, see figure 12, and L is the distance from the rotor centerplane to the screen. Hereafter we shall assume this distance to be zero.

Third but less crucial is the note made at the end of section C, that the shape of the P-gram is a function of the ratio $\omega/v$ only:

$$P_R(x,z,\psi - \omega t, v,\omega) = P_R(x,z,\psi - \omega t, \omega/v).$$

$$(II-20)$$

Let us now make a more precise definition of the burst shape function. Consider

$N_i(v) \equiv$ the number of neutrons incident upon the

chopper system with speed v, per unit length

z   per unit time t, per unit angle $\psi$.

$G(v,t) \equiv$ the number of neutrons of speed  v  which

cross the rotor centerline in time  dt

about t, which are transmitted by the

chopper system.

We shall assume $N_o$ to be independent of $\psi$, z, t.   Then

$$G(v,t) = N_i(v) \int_C P_C(x,z,\psi) \; P_R(x,z,\psi - \omega t, \; \omega/v) \; dz \; d\psi$$

$$(II-21)$$

At first glance it would appear that  G   should be a
function of the position  x   along the beam, but more careful
thought indicates that the probability that a neutron be
transmitted does not change with the position  x   at which
it is observed.   The position  x   appears in $P_C$ and $P_R$ only
to the extent that it establishes the shapes of the P-grams
at whatever position is chosen to examine them.   After the
integrations are performed the results are independent of x.
The position  x   can be chosen at will for convenience, and
here we pick it to be the rotor centerplane.

We define the burst shape function

$$P(v,t) \equiv \frac{G(v,t)}{N_i(v)} \qquad\qquad (II-22)$$

$$= \int_C P_C(x,z,\psi) \; P_R(x,z,\psi - \omega t, \omega/v) \; dz \; d\psi$$

$$(II-23)$$

P then has dimensions of length times angle.

The significance of $P(v,t)$ in reference to the $z$-$\psi$ plane of the P-gram construction is now clear: It is the total overlapping area of the collimator P-gram, $P_C = 1$ and the rotor P-gram, $P_R = 1$. This area is shaded in figure 15 and can be seen to change with time $t$, while it is a function of $\omega/v$ because the shape of the $P_R$ boundaries is dependent on $\omega/v$. The function $P(v,t)$ is related to the burst shape functions of Stone and Slovacek (2) and Marseguerra and Pauli (3) in a simple fashion. Both pairs of authors considered a unidirectional beam (that is, a perfectly collimated beam) high enough to cover the rotor slit (height $h$ as in figure 9.) In the same sense as in (II-22), let us define the burst shape function for the unidirectional beam, $P_u(v,t)$. The collimator transmission probability for a perfectly collimated beam containing $\Delta\psi$ neutrons traveling in direction $\psi = 0$ may be represented

$$P_{uc}(x,z,\psi) = \begin{cases} \Delta\psi\delta(\psi); & -h|2 \leq z \leq h|2 \\ 0 & ; \quad \text{otherwise} \end{cases}$$

This function is represented as an infinitesimally narrow strip in figure 16. Then, as in (II-23),

$$P_u(v,t) = \int_{-h/2}^{h/2} P_{uc}(x,z,\psi) \; P_R(x,z,\psi - \omega t, \omega/v) \; d\,z\,d\,\psi$$

$$= \int_{-h/2}^{h/2} \Delta\psi\delta(\psi) \; P_R(x,z,\psi - \omega t, \omega/v) \; d\,z\,d\,\psi$$

$$= \Delta\psi \int_{-h/2}^{h/2} P_R(x,z,-\omega t, \omega/v) \, dz$$

$$(II-24)$$

$P_R$ is an even function in many cases, so we shall replace $-\omega t$ by $\omega t$ in the argument of $P_R$. Since $P_R$ is unity inside the P-gram and zero outside the integral (II-24) is just the difference between z on the upper boundary of the P-gram and z on the lower boundary,

$$P_u(v,t) = \Delta\psi (z_{max}(\omega t,\omega/v) - z_{min}(\omega t,\omega/v))$$

$$(II-25)$$

This is the result of references (2) and (3), except for the normalization constant h, inserted by both pairs of authors. Using the notation of Stone and Slovacek for the burst shape function,

$$f(v,t) = \frac{1}{h} (z_{max}(\omega t,\omega/v) - z_{min}(\omega t,\omega/v))$$

$$= \frac{1}{h\Delta\psi} P_u(v,t)$$

$$(II-26)$$

Use of the P-gram construction for the calculation of burst shapes has the advantage that it enables the spatial and angular distributions to be handled in a conceptually simple way. The authors of references (2) and (3) confined themselves to calculations for unidirectional beams*,

---

*It must be noted that Stone and Slovacek did proceed to develop a Fourier series for the burst shape produced by a rotor in a beam distributed uniformly in angle and uniformly in space. Their procedure, although giving a good approximation to the correct result in many cases, did not account for spatial effects at all.

presumably because of their difficulty of including the effects of distributed beams. The P-gram construction as applied here has the advantages that spatial and angular effects are well accounted for and easily understood. Moreover, the method can be generalized to cases involving several rotors and more complex collimators. In those cases it could be the basis for a very efficient digital computer code, or in fact could lead to development of simple optical analogies.

# CHAPTER III

## A CORRESPONDENCE THEOREM

In this chapter we undertake to prove a correspondence theorem, through which the performance characteristics of similar* rotors are related, as a function of rotor angular speed, neutron speed, and rotor design parameters. Invoking this theorem will enable us to justify making calculations for simplified cases and generalizing them to more complicated and realistic cases. As a criterion for judging similarity of performance, we shall fix upon the "apparent rotor boundaries" discussed in sections IIB and IIC, (see especially figure 10). That is, we shall exhibit conditions relating rotor speed, neutron speed and rotor parameters, under which the apparent boundaries of different rotors are identical.

Let us say that we wish to construct a rotor for which the apparent boundaries are described by equations

$$F_i(x, z) = 0 \qquad\qquad (III-1)$$

where $i$ indexes the boundary surfaces of the rotor, and $(x, z)$ is the stationary coordinate system of figure 9. In section IIC, we displayed the transformation through which the boundary equations written in the rotor coordinate system $(x', z')$ of figure 9, are related to the apparent boundaries. The transformation is a function of neutron speed $v$ and rotor speed $\omega$:

---

*What is meant by "similar" will be explicitly stated below.

$$\begin{cases} x = vt \\ x = x' \cos \omega t - z' \sin \omega t \\ z = x' \sin \omega t + z' \cos \omega t \end{cases} \qquad \text{(III-2)}$$

This may be rewritten in terms of the single parameter $\gamma = \frac{\omega}{v}$, when the dummy time $t$ is replaced by the parameter $\theta = \omega t$:

$$\begin{cases} x = \theta/\gamma \\ x = x' \cos \theta - z' \sin \theta \\ z = x' \sin \theta + z' \cos \theta \end{cases} \qquad \text{(III-3)}$$

Now, if the slit boundaries are described by equations

$$f_i(x',z') = 0 \qquad \text{(III-4)}$$

in the rotor system, then the function $F_i(x,z)$ describing the apparent boundaries is given parametrically through the system

$$F_i(x,z) = 0 \quad \Longleftrightarrow \quad \begin{cases} f_i(x',z') = 0 \\ x = \theta/\gamma \\ x = x' \cos \theta - z' \sin \theta \\ z = x' \sin \theta + z' \cos \theta \end{cases}$$

$$\text{(III-5)}$$

or inversely, the rotor boundary functions are given in terms of the apparent boundary functions through

$$f_i(x',z') = 0 \quad \Longleftrightarrow \quad \begin{cases} F_i(x,z) = 0 \\ x = \theta/\gamma \\ x = x' \cos \theta - z' \sin \theta \\ z = x' \sin \theta + z' \cos \theta \end{cases}$$

$$\text{(III-6)}$$

Having now established the required transformations,
let us proceed to the proof.  Suppose we design a rotor to
produce apparent boundaries $F_i^o(x,z) = 0$ for $\gamma = \gamma_o$; then the
rotor slit boundaries will be given by

$$f_i^o (x',z') = 0 \quad \Longleftrightarrow \quad \begin{cases} F_i^o(\alpha,\beta) = 0 \\ \alpha = \theta/\gamma_o \\ \alpha = x' \cos \theta - z' \sin \theta \\ \beta = x' \sin \theta + z' \cos \theta \end{cases}$$

$$(III-7)$$

in which we have replaced dummy parameters $(x,z)$ by $(\alpha,\beta)$.
Further let us inquire what are the apparent boundaries for
this rotor for $\gamma = \gamma_1$.  They will be given by the system

$$F_i^{10}(x,z) = 0 \quad \Longleftrightarrow \quad \begin{cases} f_i^o(\xi,\eta) = 0 \\ x = \varphi/\gamma_1 \\ x = \xi \cos \varphi - \eta \sin \varphi \\ z = \xi \sin \varphi + \eta \cos \varphi \end{cases}$$

$$(III-8)$$

Here the dummy parameters $(x',z')$ have been replaced by $(\xi,\eta)$,
and the equation $f_i^o(\xi,\eta) = 0$ may be replaced by the system
(III-7), to form

$$F_i^{10}(x,z) = 0 \quad \Longleftrightarrow \quad \begin{cases} F_i^o(\alpha,\beta) = 0 \\ \alpha = \theta/\gamma_o \\ \alpha = \xi \cos \theta - \eta \sin \theta \\ \beta = \xi \sin \theta + \eta \cos \theta \\ x = \xi \cos \varphi - \eta \sin \varphi \\ z = \xi \sin \varphi + \eta \cos \varphi \\ x = \varphi/\gamma_1 \end{cases}$$

$$(III-9)$$

It is only the transformation that we are interested in, that is that part of the system which for a given $(\alpha, \beta)$ gives $(x, z)$. We may easily eliminate $(\xi, \eta)$ to obtain

$$\begin{cases} x = \alpha \cos (\varphi - \theta) - \beta \sin (\varphi - \theta) \\ z = \alpha \sin (\varphi - \theta) + \beta \cos (\varphi - \theta) \\ x = \varphi / \gamma_1 \\ \alpha = \theta / \gamma_0 \end{cases} \qquad \text{(III-10)}$$

This system may also be viewed as one which for given $(\alpha, x)$ gives $(\beta, z)$. Refer to figure 17. For each value of $x = \alpha$, we wish to compare the value of $\beta$ from the equation $F_i^0(\alpha, \beta) = 0$ (on the original apparent boundary) with the value of $z$ given by $F_i^{10}(x, z) = 0$ (on the transformed boundary). That is for each abscissa $x = \alpha$, we compare $\beta$ from $F_i^0(\alpha, \beta) = 0$ with $z$ from $F_i^{10}(x = \alpha, z) = 0$. The system (10) for the choice $x = \alpha$, gives the values of $\beta$, $z$ under the stated transformation. If $\beta$ lies on the original apparent boundary, for a choice of $\alpha$, then $z$ lies on the transformed apparent boundary for the choice $x = \alpha$. The transformation (10), for $x = \alpha$ reduces to

$$\begin{cases} \alpha = \alpha \cos (\varphi - \theta) + \beta \sin (\varphi - \theta) \\ z = \alpha \sin (\varphi - \theta) + \beta \cos (\varphi - \theta) \\ \varphi - \theta = \alpha (\gamma_1 - \gamma_0) \end{cases} \qquad \text{(III-11)}$$

which is a function of the parameter $(\gamma_1 - \gamma_0)$ only.

We may then state explicitly the following theorem:
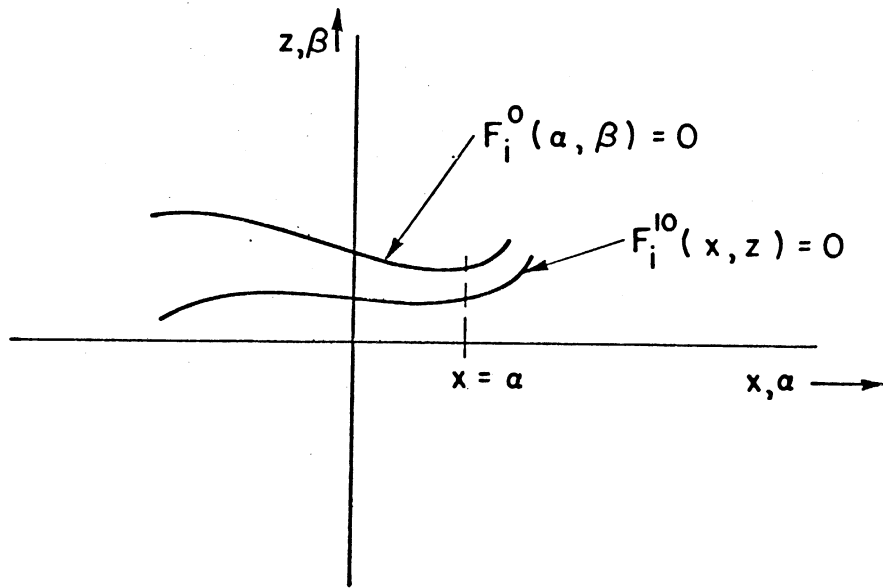
**Figure 17.** Apparent rotor boundaries $F_i^O(\alpha,\beta)$ for $\gamma_O$ and the transformed apparent boundaries $F_i^{10}(x,z)$ for $\gamma_1$, illustrating the comparison to be made between the two functions.

If rotor A produces apparent boundaries $F_i^A(x,z) = 0$ for $\gamma = \gamma_0^A$ and rotor B produces apparent boundaries $F_i^B(x,z) = F_i^A(x,z) = 0$ for $\gamma = \gamma_0^B$, then the apparent boundaries produced by A for $\gamma = \gamma_1^A$ are identical to those produced by B for $\gamma = \gamma_1^B$ if

$$\gamma_1^A - \gamma_0^A = \gamma_1^B - \gamma_0^B$$

(III-12)

This result is to be applied in the following manner. Recall that equations describing apparent slit boundaries were developed in Chapter II, for a rotor with straight slits. In the language of the theorem above, the straight slits are the apparent boundaries for infinite speed neutrons ($\gamma_0^A = 0$). We have developed expressions for the apparent boundaries for finite neutron speeds, that is for $\gamma = \gamma_1^A \geqslant 0$.

The rotors which were used in the measurements described below have curved slits, such that their apparent boundaries are straight slits for a certain value of $\gamma$, $\gamma = \gamma_0^B$. The theorem states that for neutrons with $\gamma = \gamma_1^B$, the apparent boundaries of the curved slit rotors are identical to those for the straight slit rotor, if (III-13) is satisfied.

Thus we shall use the formulae of Chapter II to describe curved slit rotors by replacing $\frac{\omega}{v}$ everywhere by

$$\frac{\omega}{v} \longrightarrow \frac{\omega}{v} - \gamma_0^B$$

(III-13)

CHAPTER IV

ANALYSIS OF THE BURST SHAPE MEASUREMENT EXPERIMENT

For the purpose of these measurements, the FNR chopper
was set up in the configuration shown in figure 18. The
beam is formed in the collimator and strikes the thermal
neutron rotor, which is assumed to turn counterclockwise.
The pulsed beam emerging from the chopper rotor contains
neutrons of many speeds, and we select those having a well-
defined speed by placing a monochromating crystal in the
beam. Neutrons travel to the detector and are counted,
having traversed a flight path of length $L_{2D}$ from the rotor
centerplane to the detector. We assume the detector to be
thin, (it is $\simeq$ 3mm. thick) and that no appreciable uncer-
tainty is introduced into the flight path in this manner.
That is, we assume that neutrons are detected instantaneously
after crossing the detector aperture. Further explanation
of the details of the experiment is given in Chapter VI,
below.

We wish to develop an expression for the counting rate
at the detector, as a function of time. Let us make the
following definitions:

H(t) dt $\equiv$ the number of neutrons crossing the
detector aperture in time dt about t.

(IV-1)

$P_C(x,z,\psi)$ $\equiv$ the probability that a neutron with
trajectory $x,z,\psi$ is transmitted through the

- 34 -

FAST-NEUTRON THERMAL-
COLLIMATOR ROTOR NEUTRON ROTOR
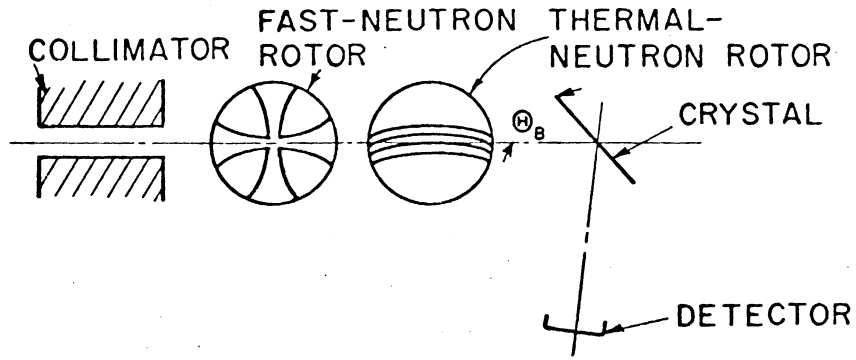


Figure 18. Schematic representation of the system used in the burst shape measurements, showing collimator, fast-neutron rotor, thermal-neutron rotor, monochromating crystal at Bragg angle $\theta_B$, and detector.
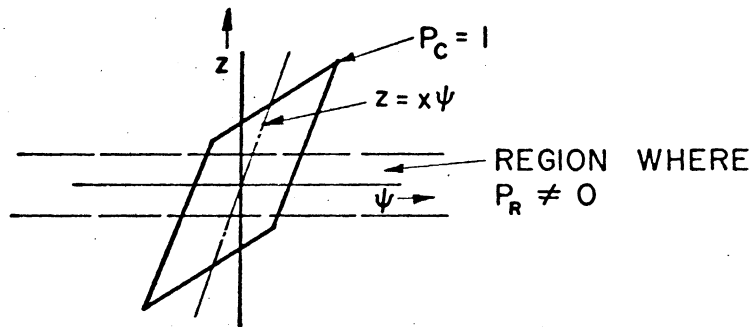


Figure 19. The collimator P-gram for a case in which the P-gram boundaries are parallel lines in the region where the rotor P-gram is not identically zero.
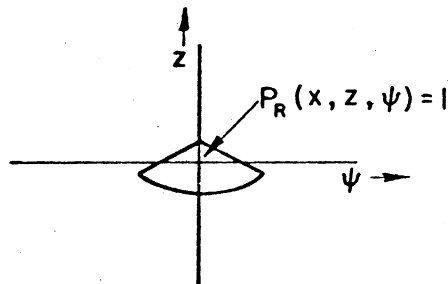


Figure 20. The P-gram for a rotor for the general case of finite velocity.

collimator.

(IV-2)

$P_R(x,z,\psi,t',\tau) \equiv$ the probability that a neutron with trajectory $x,z,\psi$ crossing the rotor center-plane at time $t'$, with flight time $\tau$, shall be transmitted through the rotor, where $\tau = \dfrac{L_{2D}}{v}$, and $L_{2D}$ is the flight path from rotor 2, the thermal neutron rotor, to the detector.

(IV-3)

$N_0(v)dv \equiv$ the number of neutrons incident on the chopper system with speed $v$ in $dv$, per unit angle $\psi$, per unit length $z$, per unit time $t$.

(IV-4)

$X(\psi,\tau) \equiv$ probability that a neutron traveling at angle $\psi$ and with flight time $\tau$ shall be reflected from the crystal.

(IV-5)

$D(t',t,\tau)dt \equiv$ the probability that a neutron of flight time $\tau$ which crosses the rotor centerplane at time $t'$ shall cross the detector aperture in time $dt$ about $t$.

(IV-6)

$P_C(x,z,\psi)$ :

$P_C$ is unity within a region of the $z$, $\psi$ plane, zero outside as in figure 19 . The shape is determined as in reference (4).

$P_R(x, z, \psi, t', \tau):$

$P_R$ is unity within a region of the $z$, $\psi$ plane and zero
outside. The region $P_R = 1$ moves in the $z - \psi$ plane,

$P_R(x, z, \psi, t', \tau) = P_R(x, z; \psi - \omega t', \tau)$ and has a shape determined
by the method of chapters II and III. See figure 20 .

$X(\psi, \tau):$

A neutron is reflected if it satisfies the Bragg con-
dition:

$$\lambda = 2d \sin (\theta_B + \psi) \qquad (IV-7)$$

We may write this as a condition on the flight time as well
as on the wavelength:

$$\lambda = \frac{K}{v} ; \qquad K = a \text{ constant} \qquad (IV-8)$$

$$\tau = \frac{L_{2D}}{v} ; \qquad \tau = \frac{L_{2D}}{K} \lambda \qquad (IV-9)$$

$$\tau = \frac{L_{2D}}{K} 2d \sin (\theta_B + \psi) \qquad (IV-10)$$

Recall that $\psi$ is small, so that $\sin \psi \simeq \psi$, $\cos \psi \simeq 1$; we
write therefore

$$\tau = \frac{2dL_{2D}}{K} \left[ \sin \theta_B \cos \psi + \cos \theta_B \sin \psi \right]$$

$$\tau \cong \frac{2dL_{2D}}{K} \left[ \sin \theta_B + \psi \cos \theta_B \right]$$

$$= \frac{2dL_{2D}}{K} \sin \theta_B \left[ 1 + \psi \cot \theta_B \right] \qquad (IV-11)$$

The mean angle of the $\psi$ distribution is $\psi = 0$, and this
gives the mean flight time $\tau_B$ reflected from the crystal,

$$\tau_B = \frac{2dL_{2D}}{K} \sin \theta_B \qquad (IV-12)$$

- 38 -

thus (11) may be written

$$\tau = \tau_B \left[ 1 + \psi \cot \theta_B \right] \qquad (IV-13)$$

The neutrons are reflected with an efficiency $R(\tau)$, related to the crystal reflectivity of Bacon[5] and having the dimensions of flight time. Thus

$$X(\psi,\tau) = R(\tau) \, \delta(\tau - \tau_B \left[ 1 + \cot \theta_B \psi \right] ) \qquad (IV-14)$$

$D(t',t,\tau)$:

Neutrons crossing a point at time $t'$ always reach a downstream point at distance $L_{2D}$ at a time $t$ given by $t = t' + \tau$, so

$$D(t', t, \tau) = \delta(t - t' - \tau) \qquad (IV-15)$$

As defined, these functions combine to give the measured counting rate

$$H(t)dt = \int N_o(\tau) \, P_C(x,z,\psi) R(\tau) \delta(\tau-\tau_B \left[ 1 + \psi \cot \theta_B \right] ) \text{ (x)}$$

$$\text{(x)} \; P_R(x,z,\psi-\omega t',\tau)\delta(t-t'-\tau) \; d\,z \, d\,\psi \, d\,\tau \, dt' \, dt \qquad (IV-16)$$

The first $\delta$-function under the integral takes care of the $\tau$-integration, replacing $\tau$ wherever it appears by $\tau = \tau_B(1 + \psi \cot \theta_B)$. However, we may consider $R(\tau) \, N(\tau)$ to be slowly-varying functions of $\tau$, and therefore evaluate $\tau$ at its mean value, $\tau_B$, in those functions. Similarly,

(5) Bacon,"Neutron Diffraction," p. 64, 82., Oxford University Press, London (1955)

$P_R$ varies slowly with respect to $\tau$ in its last argument and the same is done there

$$H(t)dt = \int N_0(\tau_B) \, P_C(x,z,\psi)R(\tau_B)P_R(x,z,\psi-\omega t',\tau_B)$$
$$\delta(t-t'-\tau_B \left[1 + \cot \theta_B \psi\right] ) \, d\,z\,d\,\psi\,d\,t'\,dt$$

$$(IV-17)$$

The t'-integration is easily performed, requiring that we evaluate t' at $t' = t - \tau_B(1 + \cot \theta_B \psi)$:

$$H(t)dt = \int N_0(\tau_B)P_C(x,z,\psi)P_R(x,z,\psi - \omega(t - \tau_B \left[1 + \cot \theta_B \psi\right]),\tau_B)$$
$$d\,z\,d\,\psi\,dt \qquad\qquad (IV-18)$$

$$= \int N_0(\tau_B)P_C(x,z,\psi)R(\tau_B)P_R(x,z,\psi \left[1+\omega\tau_B\cot\theta_B\right]-\omega(t-\tau_B),\tau_B)$$
$$d\,z\,d\,\psi$$

$$(IV-19)$$

In the same spirit as in the case of the burst shape function P(v,t) of Chapter II, equation (II-23), we normalize this function to unit incident intensity and unit reflectivity,

$$M(\theta_B,t) \equiv \frac{H(t)}{N_0(\tau_B)\,R(\tau_B)}$$

$$= \int P_C(x,z,\psi)P_R(x,z,\psi\,(1 + \omega\,\tau_B\cot\,\theta_B)-\omega(t-\tau_B),\tau_B)$$
$$d\,z\,d\,\psi$$

$$(IV-20)$$

The function $M(\theta_B,t)$ will be referred to as the "measured function." Note the factor $(1 + \omega\,\tau_B\cot\,\theta_B)$ multiplying $\psi$ in $P_R$.

The rate of motion of the rotor P-gram across the $z - \psi$ plane can be obtained by following a point on the P-gram,

$$\psi(1 + \omega\tau_B \cot \theta_B) - \omega(t - \tau_B) = \text{constant}$$

$$\frac{d \psi}{d t} = \frac{\omega}{(1 + \omega\tau_B \cot \theta_B)} \qquad \text{(IV-21)}$$

Say the factor $(1 + \omega\tau_B \cot \theta_B)$ is greater than unity. Then the rotor P-gram moves across the $z - \psi$ plane more slowly in this case than in the case of the burst shape function. Thus the rotor P-gram moves more slowly through the collimator P-gram; the effect is to broaden the burst by broadening the contribution of the collimator P-gram.

What does the multiplier on $\psi$ do to the P-gram picture of the formation of the burst? Figure 21 shows the case for a perfectly monochromatic beam.

Figure 22 shows how this picture is modified by the presence of the factor $(1 + \omega\tau_B \cot \theta_B)$ arising due to the fact that a crystal monochromator was used. We make a minor change in the form of (IV-20), in terms of which to discuss this modification. For this, define a new dummy variable

$$\xi = \psi(1 + \omega\tau_B \cot \theta_B) \; ; \; d\psi = \frac{d\xi}{1 + \omega\tau_B \cot \theta_B}$$

$$M(\theta_B, t) = \int P_C\left(x, z, \xi / (1 + \omega\tau_B \cot \theta_B)\right) \times$$

$$\times P_R\left(x, z, \xi - \omega(t - \tau_B), \tau_B\right) \frac{d z \, d \xi}{(1 + \omega\tau_B \cot \theta_B)}$$

$$\text{(IV-22)}$$

In a $z - \xi$ plane, the rotor P-gram is undeformed by the factor $(1 + \omega\tau_B \cot \theta_B) = \alpha$, although the collimator P-gram
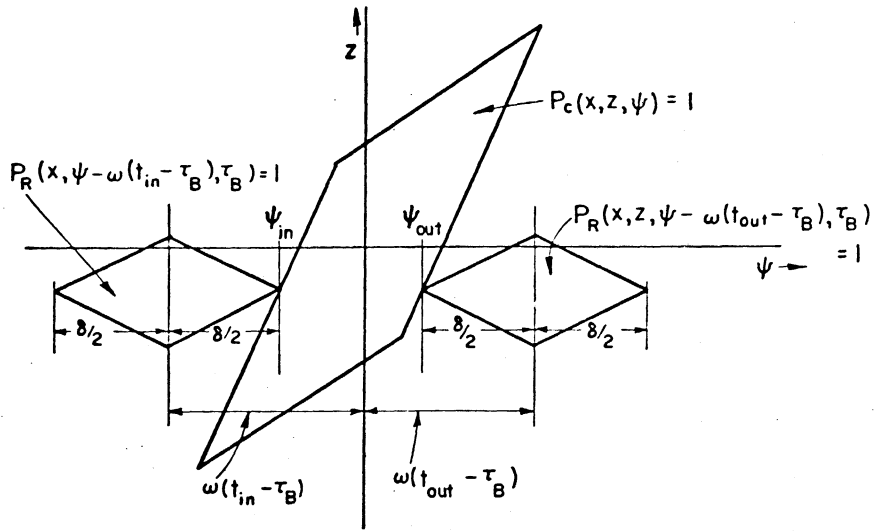
Figure 21. The P-gram picture showing the collimator P-gram undistorted, and the rotor P-gram at two instants of time; $t_{in}$ at which the burst just begins, and $t_{out}$ at which the burst just ends.
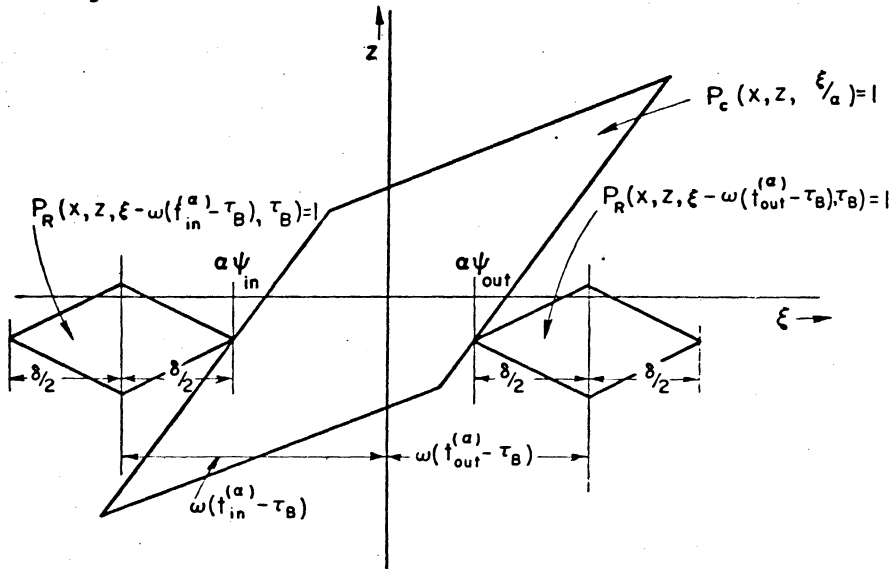


Figure 22. The P-gram picture showing the collimator P-gram distorted by the factor $\alpha > 1$, and the rotor P-gram at two instants of time; $t_{in}^{(\alpha)}$ at which the burst just begins, and $t_{out}^{(\alpha)}$ at which the burst just ends.

is now modified. Also, the rate of motion of the rotor P-gram across the z - $\xi$ plane is

$$\frac{d\xi}{dt} = \omega \qquad\qquad (\text{IV-23})$$

In addition, for $\alpha = 0$,

$$M_{\alpha=0}(\theta_B, t) = \int P_C(x, z, \psi) P_R(x, z, -\omega(t-\tau_B), \tau_B) d\,z\,d\,\psi$$

$$= \int \left[ \int P_C(x, z, \psi) d\,\psi \right] P_R(x, z, -\omega(t-\tau_B), \tau_B)\,d\,z \qquad (\text{IV-24})$$

If $\left[ \int P_C(x, z, \psi) d\,\psi \right]$ is constant with respect to z in the range where $P_R \neq 0$, then $M_{\alpha=0}(\theta_B, t)$ is proportional to the function $P_u(v, t)$ of equation (II-24).

Further, the total number of neutrons per burst for $M(\theta_B, t)$ is

$$\int M(\theta_B, t) dt = \int P_C(x, t, \psi) P_R(x, z, \alpha\psi - \omega(t-\tau_B), \tau_B) d\,z\,d\,\psi\,d\,t \qquad (\text{IV-25})$$

where $\alpha = (1 + \omega\,\tau_B \cot \theta_B)$. Put $\alpha\psi - \omega(t-\tau_B) = \mu$, $d\mu = \omega dt$ then

$$M(\theta_B, t) dt = \frac{1}{\omega} \int P_C(x, z, \psi) d\,\psi\, P_R(x, z, \mu, \tau_B)\,d\,\mu\,d\,z \qquad (\text{IV-26})$$

which is independent of $\alpha$, and therefore remains finite for all values of $\alpha$. (One might expect that as $\alpha \to 0$, as it may, the neutron intensity would approach zero.) This result corresponds to that for the monochromatic beam, that is for $P(v, t)$.

Still further to illustrate the effect of the presence

of the factor $\alpha$, refer to figure 21 , for $o=1$ (for $P(v,t)$).

The burst begins at the time $t_{in}$ such that

$$\omega(t_{in}-\tau_B) = -(\delta/2 + \psi_{in}) \; ; \; \omega t_{in} = \tau_B -(\delta/2 + \psi_{in})$$

$$(IV-27)$$

and ends at time $t_{out}$ such that

$$\omega(t_{out}-\tau_B) = (\delta/2 + \psi_{out}) \; ; \; \omega t_{out} = \tau_B +(\delta/2 + \psi_{in})$$

$$(IV-28)$$

The width of the burst is thus

$$t_{out}-t_{in} = \frac{1}{\omega} (\delta + \psi_{in} + \psi_{out}) \qquad (IV-29)$$

where $\delta$ is due to the rotor, and $(\psi_{in} + \psi_{out})$ is due to the collimator.

Referring to figure 22 , for $\alpha > 1$, we see that the collimator P-gram on a $z - \xi$ plane is broadened. Thus, proceeding as above, the width is

$$t_{out}^{(\alpha)} - t_{in}^{(\alpha)} = \frac{1}{\omega} (\delta + \alpha(\psi_{in} + \psi_{out}))$$

$$(IV-30)$$

illustrating the broadening effect as one which increases the collimator contribution to the width by the factor $\alpha$.

Further and more complete results will be developed in the following chapter.

CHAPTER V

CALCULATION OF THE BURST SHAPE

In the preceding, expressions were developed for the functions $P(v,t)$ and $M(\theta_B,t)$, exhibiting them as integrals involving the collimator and rotor transmission probability. Equations describing the apparent boundaries of the P-gram for a straight-slit rotor were derived. It was shown how to apply those results to the description of a class of similar curved-slit rotors. Little has been said concerning the collimator P-gram itself, since its shape can be determined by the methods of reference (4). The effect of the monochromating crystal has been shown to be one which broadens the collimator P-gram in the $\psi$ dimension by the factor $\alpha = (1 + \omega \tau_B \cot \theta_B)$.

Two approaches could be followed from this point: To perform the actual calculations using a computer, or to develop formulae for hand calculation. For more complex analyses than the present, the computer is the only reasonable choice, and the techniques described above should form the basis for a very efficient program. However, the experiment which we propose to analyze is fairly uncomplicated and we can expect hand calculations to be quite satisfactory, as well as more general. We proceed in the following to develop formulae suited to hand calculation.

It is the case in many systems that the collimator P-gram has the special property illustrated in figure 19.

Here the collimator P-gram boundaries are particularly simple in the important region traversed by the rotor P-gram:

$$P_C(x, z, \psi) = \begin{cases} 1; & \text{if} \quad -\psi_0 + z/S \leqslant \psi \leqslant \psi_0 + z/S \\ 0; & \text{otherwise} \end{cases} \qquad \text{(V-1)}$$

Where $\psi_0$ is the maximum angle transmitted by the collimator through the point $z = 0$, and S is the distance from the screen to the aperture in the collimator defining the collimator P-gram boundary. In terms of the variable $\xi = \alpha\psi$,

$$P_C(x, z, \xi/\alpha) = \begin{cases} 1; & \text{if} \quad -\alpha\psi_0 + \alpha z/S \leqslant \xi \leqslant \alpha\psi_0 + \alpha z/S \\ 0; & \text{otherwise} \end{cases}$$

$$\text{(V-1')}$$

For the range of z over which (V-1) holds, $P_C$ may be represented therefore

$$P_C(x, z, \psi) = \int_{-\psi_0}^{\psi_0} \delta(z/S - \psi + \psi') \, d\psi' \qquad \text{(V-2)}$$

or

$$P_C(x, z, \xi/\alpha) = \int_{-\alpha\psi_0}^{\alpha\psi_0} \delta(\alpha z/S - \xi + \xi') \, d\xi' \qquad \text{(V-2')}$$

Recalling equation (IV-22),

$$M(\theta_B, t) = \frac{1}{\alpha} \int P_C(x, z, \xi/\alpha) \, P_R(x, z, \xi-\omega t, \tau_B) \, dz \, d\xi \qquad \text{(IV-22)}$$

Applying (V-2'), we have

$$
M(\theta_B, t) = \frac{1}{\alpha} \int_{-\alpha \psi_o}^{\alpha \psi_o} \delta(\alpha z/S - \xi + \xi') d\xi' P_R(x, z, \xi - \omega t, \tau_B) d z d \xi \qquad (V-3)
$$

Putting $\xi = \eta + \alpha z/S + \omega t$, $d\xi = d\eta$, this becomes

$$
M(\theta_B, t) = \frac{1}{\alpha} \int_{-\alpha \psi_o}^{\alpha \psi_o} \delta(\xi' - \eta - \omega t) P_R(x, z, \eta + \alpha z/S, \tau_B) d\xi' d\eta d z \qquad (V-4)
$$

and further changing $\xi'' = \xi' - \omega t$, $d\xi'' = d\xi'$

$$
M(\theta_B, t) = \frac{1}{\alpha} \int_{-\alpha \psi_o - \omega t}^{\alpha \psi_o - \omega t} \delta(\xi'' - \eta) P_R(x, z, \eta + \alpha z/S, \tau_B) d\xi'' d\eta d z \qquad (V-5)
$$

The function $P_R(x, z, \eta + \alpha z/S, \tau_B)$ looks much like the previous rotor P-gram, but is deformed, as in figures 23 and 24. The integral

$$
\int P_R(x, z, \eta + \alpha z/S, \tau_B) \delta(\xi'' - \eta) d\eta d z \qquad (V-6)
$$

is interpretable as the length of a vertical line passing through $\eta = \xi''$, which lies inside the deformed rotor P-gram. This interpretation is the same as that given in section IIE, in showing the correspondence between the P-gram burst shape calculation, and the calculations of Stone and Slovacek,

$$0 \leq \beta \leq \frac{1}{4}$$

(b) $z = R\left(-\dfrac{\eta}{\rho} - \dfrac{2\delta\beta}{\rho^2} + \dfrac{2}{\rho}\sqrt{\dfrac{\beta\delta}{\rho}}\sqrt{\dfrac{\delta\rho}{2} + \dfrac{\beta\delta}{\rho} + \eta}\right)$

(a) $z = \dfrac{R}{1-\rho}(\eta + \delta/2 + \beta\delta)$

(c) $z = \dfrac{R}{1+\rho}(-\eta + \delta/2 + \beta\delta)$

$\delta(-2\beta + \beta\rho - \rho/2)$    $\delta(2\beta + \beta\rho - \rho/2)$

$-\delta(\beta\rho + 1/2)$    $\delta(\rho/2 - \beta\rho)$    $\delta(-\beta\rho + 1/2)$    $\eta \rightarrow$

(d) $z = \dfrac{R}{1-\rho}\left(\eta - \delta/2 + \beta\delta\right)$

(e) $z = \dfrac{R}{1+\rho}\left(-\eta - \delta/2 + \beta\delta\right)$
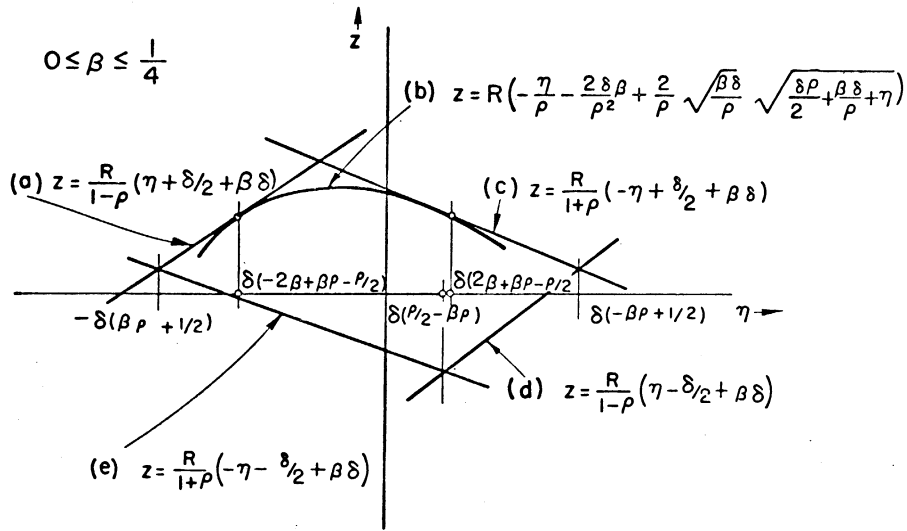
Figure 23. The rotor P-gram $P_R(x, z, \eta + \alpha \frac{z}{S}, v/\omega)$ showing the effect of the argument $\eta + \alpha$ z/S in distorting the P-gram. Drawn for $0 \leqslant \beta \leqslant 1/4\,(\beta = R^2\omega/hv)$.

$$\frac{1}{4} \leq \beta \leq 1$$

(f) $z = R\left(-\dfrac{\eta}{\rho} - \dfrac{2\delta\beta}{\rho^2} + \dfrac{2}{\rho}\sqrt{\dfrac{\beta\delta}{\rho}}\sqrt{\dfrac{\delta\rho}{2} + \dfrac{\beta\delta}{\rho} + \eta}\right)$

$\delta(-2\sqrt{\beta} + 2\beta - 2\rho\sqrt{\beta} + \rho/2 + \beta\rho)$    $\delta(2\sqrt{\beta} - 2\beta - 2\rho\sqrt{\beta} + \rho/2 + \beta\rho)$

$\eta \rightarrow$

(h) $z = \dfrac{R}{1+\rho}\left(-\eta - \delta/2 - \beta\delta\right)$

(g) $z = \dfrac{R}{1+\rho}(\eta - \delta/2 + \beta\delta)$
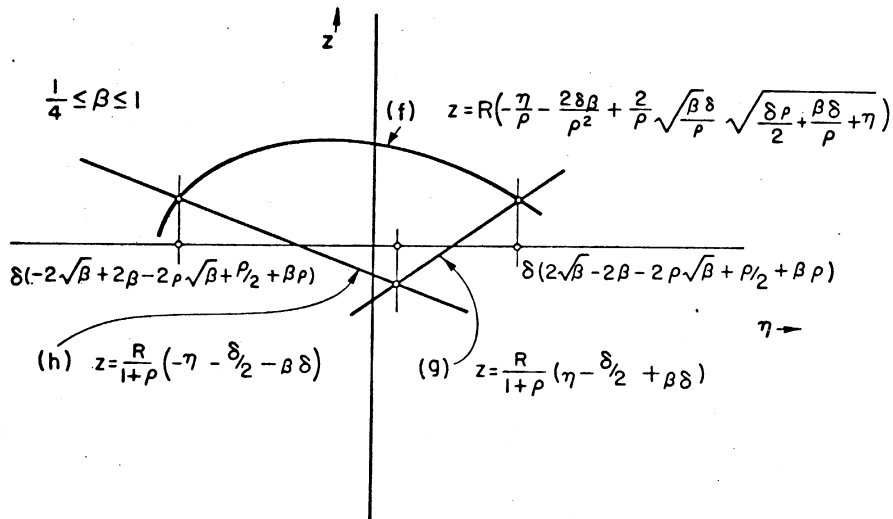
Figure 24. The distorted rotor P-gram $P_R(x, z, \eta + \alpha$ z/S,v/$\omega$) drawn for $1/4 \leqslant \beta \leqslant 1$ $(\beta = R^2\omega/hv)$.

and of Marseguerra and Pauli. The difference here is in the deformation of the rotor P-gram, and arises due to the correct inclusion of the effect of the collimator. In similar fashion to the interpretation of section IIE, we may write this length as the difference between z on the upper boundary of the deformed P-gram, and z on its lower boundary:

$$\int P_R(z,\eta + \alpha \frac{z}{s}, \omega/v) \; \delta(\xi''-\eta) d\eta \; d \; z = z_u(\xi'') - z_\lambda(\xi'')$$

(V-7)

The burst shape function, from (4) is then

$$M(\theta_B,t) = \int_{-\alpha\psi_o-\omega t}^{\alpha\psi_o-\omega t} \left[ z_u(\xi'') - z_\lambda(\xi'') \right] d\xi''$$

(V-8)

Further, let us define these integrals

$$\int_{\alpha_u}^{\eta} z_u(\eta') \; d\eta' \; = \; z_u(\eta)$$

$$\int_{\alpha_\lambda}^{\eta} z_\lambda(\eta') \; d\eta' \; = \; z_\lambda(\eta)$$

(V-9)

Here $\alpha_u$ and $\alpha_\lambda$ are irrelevant limits, chosen to simplify the work. We shall calculate these last-defined functions $Z_u(\eta)$ and $Z_\lambda(\eta)$, in terms of which

$$M(\theta_B,t) = Z_u(\alpha\psi_o-\omega t) - Z_u(-\alpha\psi_o-\omega t) - Z_\lambda(\alpha\psi_o-\omega t) + Z_\lambda(-\alpha\psi_o-\omega t)$$

$$= \Delta Z \; (\alpha\psi_o - \omega t) - \Delta Z \; (-\alpha\psi_o - \omega t)$$

(V-10)

The calculation is performed as outlined above. The boundary equations of the deformed P-gram, $P_R(x,z,\eta+\alpha\frac{z}{s},\tau_B)= 1$

are first computed. These equations are displayed in tables Ia (for $\frac{4P^2\omega}{h} \leqslant v \leqslant \infty$ ) and Ib (for $\frac{R^2\omega}{h} \leqslant v \leqslant \frac{4R^2\omega}{h}$), and Figures 23 and 24. The results are presented in terms of reduced variables

$$\rho = \alpha \frac{R}{S}$$

$$\delta = \frac{h}{R}$$

$$\beta = \frac{R^2\omega}{hv} \tag{V-11}$$

The functions $Z_u(\eta)$ and $Z_{\ell}(\eta)$ are calculated from $z_u(\eta)$ and $z_{\ell}(\eta)$ on these boundaries. The work of the actual calculation is algebraically involved but altogether trivial, requiring integration of elementary forms. Therefore, only the results are presented. Table IIa contains the function $z_u(\eta)$ for $\frac{4R^2\omega}{h} \leqslant v \leqslant \infty$, IIb for $\frac{R^2\omega}{h} \leqslant v \leqslant \frac{4R^2\omega}{h}$. Table IIIa contains $z_{\ell}(\eta)$ for $\frac{4R^2\omega}{h} \leqslant v \leqslant \infty$, IIIb for $\frac{R^2\omega}{h} \leqslant v \leqslant \frac{4R^2\omega}{h}$.

As it happens, a removable singularity exists at $\rho = 0$ in the functions (V-30) and (V-34). As a consequence, for small values of $\rho$, these equations do not lend themselves to easy calculation. To simplify the numerical calculations it is appropriate to approximate these equations with an expansion in powers of $\rho$. The development of the expansion is straightforward and is presented as an Appendix, where the notation is also clarified. The result is

$$z_u(\eta) = R\left\{ -\frac{\delta^2\rho}{8} - \frac{4}{3}\frac{\beta^2\delta^2}{\rho^3} \sum_{n=3}^{\infty} \sum_{k=0}^{[n/2]} \frac{(-3/2)n-k}{k! \ (n-2k)!}(-1)^n \right.$$

$$\left. (-\frac{1}{2\beta})^k (\frac{\eta}{\beta\delta})^{n-2k} \rho^n \right\} \tag{A-11}$$

the expansion being the same for both (V-30) and (V-34).

The ranges of applicability are the same as for the original

formulae, of course.

TABLE V - 1a    For $0 \leq \beta \leq \frac{1}{4}$    (or $\frac{4R^2\omega}{h} \leq \nu \leq \infty$ )

| Eq. No. | Boundary (See Fig.16a) | $z_u(\eta)$ or $z_\ell(\eta)$ | Range |
|---|---|---|---|
| (V-12) | (a) | $z_u = \dfrac{R}{1-\rho}(\eta + \delta/2 + \beta\delta)$ | $-\delta(\beta\rho + \frac{1}{2}) \leq \eta \leq \delta(-2\beta + \beta\rho - \rho/2)$ |
| (V-13) | (b) | $z_u = R(-\dfrac{\eta}{\rho} - \dfrac{2\delta\beta}{\rho^2} + \dfrac{2}{\rho}\sqrt{\dfrac{\beta\delta}{\rho}}\sqrt{\dfrac{\delta\rho}{2} + \dfrac{\beta\delta}{\rho} + \eta}\ )$ | $\delta(-2\beta + \beta\rho - \rho/2) \leq \eta \leq \delta(2\beta + \beta\rho - \rho/2)$ |
| (V-14) | (c) | $z_u = \dfrac{R}{1+\rho}(-\eta + \delta/2 + \beta\delta)$ | $\delta(2\beta + \beta\rho - \rho/2) \leq \eta \leq \delta(-\beta\rho + 1/2)$ |
| (V-15) | (d) | $z_\ell = \dfrac{R}{1-\rho}(\eta - \delta/2 + \beta\delta)$ | $\delta(\rho/2 - \beta\rho) \leq \eta \leq \delta(-\beta\rho + 1/2)$ |
| (V-16) | (e) | $z_\ell = \dfrac{R}{1+\rho}(-\eta - \delta/2 + \beta\delta)$ | $-\delta(\beta\rho + 1/2) \leq \eta \leq \delta(\rho/2 - \beta\rho)$ |

TABLE V - 1b  For  $\frac{1}{4} \le \beta \le 1$  or  $(\frac{R^2\omega}{h} \le v \le \frac{4R^2\omega}{h})$

| Eq. No. | Boundary (See Fig.16b) | $z_u(\eta)$ or $z_\ell(\eta)$ | Range |
|---|---|---|---|
| (V-17) | (f) | $z_u = R(-\frac{\eta}{\rho} - \frac{2\delta\beta}{\rho^2} + \frac{2}{\rho}\sqrt{\frac{\beta\delta}{\rho}}\sqrt{\frac{\delta\rho}{2} + \frac{\beta\delta}{\rho} + \eta})$ | $q_1 \le \eta \le q_2$ |
| (V-18) | (g) | $z_\ell = \frac{R}{1-\rho}(\eta - \delta/2 + \beta\delta)$ | $\delta(\rho/2 - \beta\rho) \le \eta \le q_2$ |
| (V-19) | (h) | $z_\ell = \frac{R}{1+\rho}(-\eta - \delta/2 + \beta\delta)$ | $q_1 \le \eta \le \delta(\rho/2 - \beta\rho)$ |

$q_1 = \delta(-2\sqrt{\beta^2 + 2\beta} - 2\rho\sqrt{\beta + \rho/2 + \beta\rho})$

$q_2 = \delta(2\sqrt{\beta^2 - 2\beta} - 2\rho\sqrt{\beta + \rho/2 + \beta\rho})$

TABLE V - 2a  For  $0 \leq \beta \leq 1/4$  (or  $\frac{4R^2\omega}{h} \leq \nu \leq \infty$ )

$$\alpha_\ell = \delta(\rho/2 - \beta\rho)$$

| Equation Number | $z_\ell(\eta)$ | Range |
|---|---|---|
| (V-20) | $-\dfrac{R\delta^2}{2}(1/4 - \beta)(1 - \rho)$ | $\eta \leq -\delta(\beta\rho + 1/2)$ |
| (V-21) | $\dfrac{R}{1 + \rho}\left[\dfrac{\eta^2}{2} + \delta(1/2 - \beta)\eta - \dfrac{\delta^2}{2}(\rho^2 + 2\rho)\left(\dfrac{1}{2} - \beta\right)^2\right]$ | $-\delta(\beta\rho + 1/2) \leq \eta \leq \delta(\rho/2 - \beta\rho)$ |
| (V-22) | $\dfrac{R}{1 - \rho}\left[-\dfrac{\eta^2}{2} + \delta(1/2 - \beta)\eta + \dfrac{\delta^2}{2}(\rho^2 - 2\rho)\alpha \right.$ $\left. (\alpha)(1/2 - \beta)^2\right]$ | $\delta(\rho/2 - \beta\rho) \leq \eta \leq \delta(1/2 - \beta\rho)$ |
| (V-23) | $\dfrac{R\delta^2}{2}(1/4 - \beta)(1 - \rho)$ | $\eta \geq \delta(1/2 - \beta\rho)$ |

**TABLE V - 2b**    For    $\frac{1}{4} \leq \beta \leq 1$    (Or $\frac{R^2\omega}{h} \leq v \leq \frac{4R^2\omega}{h}$)

$$\alpha_\ell = \delta(\rho/2 - \beta\rho)$$

| Equation Number | $z_\ell(\eta)$ | Range |
|---|---|---|
| (V-24) | $-2R\delta^2(1+\rho)\sqrt{\beta}(\sqrt{\beta}-1)(\sqrt{\beta}-1/2)$ | $\eta \leq q_1$ |
| (V-25) | $\dfrac{R}{1+\rho}\left[\dfrac{\eta^2}{2} + \delta(1/2-\beta)\eta - \dfrac{\delta^2}{2}(\rho^2+2\rho)(1/2-\beta)^2\right]$ | $q_1 \leq \eta \leq \delta(\rho/2 - \beta\rho)$ |
| (V-26) | $\dfrac{R}{1-\rho}\left[-\dfrac{\eta^2}{2} + \delta(1/2-\beta)\eta + \dfrac{\delta^2}{2}(\rho^2 - 2\rho)(1/2-\beta)^2\right]$ | $\delta(\rho/2 - \beta\rho) \leq \eta \leq q_2$ |
| (V-27) | $2R\delta^2(1-\rho)\sqrt{\beta}(\sqrt{\beta}-1)(\sqrt{\beta}-1/2)$ | $\eta \geq q_2$ |

$$q_1 = \delta(-2\sqrt{\beta}+2\beta - 2\rho\sqrt{\beta}+\rho/2+\beta\rho)$$

$$q_2 = \delta(2\sqrt{\beta}-2\beta - 2\rho\sqrt{\beta}+\rho/2+\beta\rho)$$

**TABLE V – 3a,  For  $0 \leq \beta \leq \frac{1}{4}$  (or  $\frac{4R^2\omega}{h} \leq \nu \leq \infty$ )**

$$\alpha_u = -\delta\rho/2$$

| Equation Number | $z_u(\eta)$ | Range |
|---|---|---|
| (V-28) | $\dfrac{R\delta^2}{2}\left[\dfrac{1}{4}(1-\rho) + \beta - \dfrac{4}{3}\beta^2 + \beta^2\rho\right]$ | $\eta \leq -\delta(\beta\rho + 1/2)$ |
| (V-29) | $\dfrac{R}{1-\rho}\left[-\dfrac{1}{2}\eta^2 - \delta(\beta + 1/2)\eta - \delta^2\left(\dfrac{\beta\rho}{2} + \dfrac{2}{3}\beta^2 - \dfrac{1}{6}\beta^2\rho + \dfrac{\rho}{4} - \dfrac{\rho^2}{8}\right)\right]$ | $-\delta(\beta\rho + 1/2) \leq \eta \leq \delta(-2\beta - \beta\rho + \dfrac{\rho}{2})$ |
| (V-30) | $R\left\{\dfrac{\eta^2}{2\rho} + \dfrac{2\delta\beta}{\rho}\eta - \dfrac{4}{3\rho}\sqrt{\dfrac{\delta\delta}{\rho}}\left(\dfrac{\delta\rho}{2} + \dfrac{\beta\delta}{\rho} + \eta\right)^{3/2} - \delta^2\left(\dfrac{\rho}{8} - \dfrac{\beta}{\rho} - \dfrac{4}{3}\dfrac{\beta^2}{\rho^3}\right)\right\}$ | $\delta(-2\beta - \beta\rho - \rho/2) \leq \eta \leq \delta(2\beta + \beta\rho - \rho/2)$ |
| (V-31) | $\dfrac{R}{1+\rho}\left[\dfrac{1}{2}\eta^2 - \delta(\beta + 1/2)\eta - \delta^2\left(\dfrac{\beta\rho}{2} - \dfrac{2}{3}\beta^2 - \dfrac{1}{6}\beta^2\rho + \dfrac{\rho}{4} + \dfrac{\rho^2}{8}\right)\right]$ | $\delta(2\beta + \beta\rho - \dfrac{\rho}{2}) \leq \eta \leq \delta(-\beta\rho + 1/2)$ |
| (V-32) | $-\dfrac{R\delta^2}{2}\left[\dfrac{1}{4}(1+\rho) + \beta - \dfrac{4}{3}\beta^2 - \beta^2\rho\right]$ | $\eta \geq \delta(-\beta\rho + 1/2)$ |

TABLE V - 3b  For  $\frac{1}{4} \leqslant \beta \leqslant 1$  (Or $\frac{R^2\omega}{h} \leqslant v \leqslant \frac{4R^2\omega}{h}$)

$$\alpha_u = \delta\rho/2$$

| Equation Number | $z_u(\eta)$ | Range |
|---|---|---|
| (V-33) | $R\delta^2\left[\dfrac{\rho}{2}(2\sqrt{\beta}-\beta)(2\sqrt{\beta}-\beta-1)+\dfrac{2}{3}(\sqrt{\beta}-\beta)(2\sqrt{\beta}-\beta+1/2)\right]$ | $\eta \leqslant q_1$ |
| (V-34) | $R\left[\dfrac{\eta^2}{2\rho}+\dfrac{2\delta\beta}{\rho^2}\eta-\dfrac{4}{3\rho}\sqrt{\dfrac{\beta\delta}{\rho}}\left(\dfrac{\delta\rho}{2}+\dfrac{\beta\delta}{\rho}+\eta\right)^{3/2}-\delta^2(\rho/8-\beta/\rho-\dfrac{4}{3}\dfrac{\beta^2}{\rho^3})\right]$ | $q_1 \leqslant \eta \leqslant q_2$ |
| (V-35) | $R\delta^2\left[\dfrac{\rho}{2}(2\sqrt{\beta}-\beta)(2\sqrt{\beta}-\beta-1)-\dfrac{2}{3}(\sqrt{\beta}-\beta)(2\sqrt{\beta}-\beta+1/2)\right]$ | $\eta \geqslant q_2$ |

$$q_1 = \delta(-2\sqrt{\beta}+2\beta-2\rho\sqrt{\beta}+\rho/2+\beta\rho)$$

$$q_2 = \delta(2\sqrt{\beta}-2\beta-2\rho\sqrt{\beta}+\rho/2+\beta\rho)$$

CHAPTER VI

DESCRIPTION OF THE EXPERIMENTAL ARRANGEMENT

In this section are described several experiments per-
formed at the University of Michigan machine which are subject
to analysis by the methods developed above. The physical
configuration of the machine during these measurements is
depicted in figure 25; the signal flow system is shown in
figure 26. A brief description of the significant aspects
of each component is given below, but we now undertake to
discuss the operation of the entire system.

Two rotors were actually placed in the beam; nearest the
collimator (A)* exit was a fiberglass-resin rotor (B),
referred to hereafter as rotor 1,and further downstream was
the chopping rotor (C) referred to as rotor 2. Rotor 1
produces a very broad burst, that is a burst of relatively
very long duration, four times per revolution and was run
at one-fourth the speed of rotor 2, in phase with the chop-
ping rotor so as not to interfere with the beam chopped by
rotor 2. Its effect was to reduce the background at the
detector due to fast (i.e., epicadmium) neutrons, which are
not greatly attenuated by the chopping rotor. The neutrons
striking rotor 2 are chopped by this high-resolution rotor
into a narrow burst, which contains neutrons of many speeds.

In the absence of a device to select only one speed

*Letters in parenthesis indicate the section below in which
the system component referred to is described.

- 57 -

COLLIMATOR    ROTOR I    ROTOR 2    CRYSTAL

$59 \frac{1}{2}'' = L_{2D}$

4.75"    2.00"

$\Theta_B$

$2\Theta_B$

108"    54"

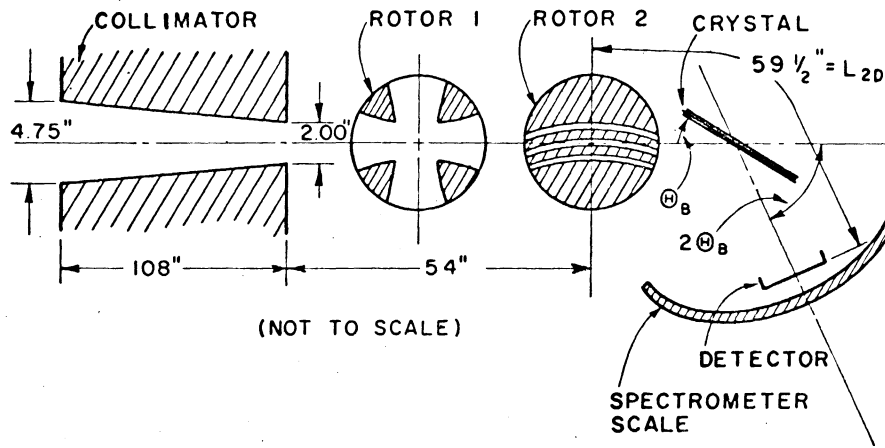(NOT TO SCALE)

DETECTOR

SPECTROMETER
SCALE

Figure 25. Schematic representation of the machine configuration during the burst shape measurements.
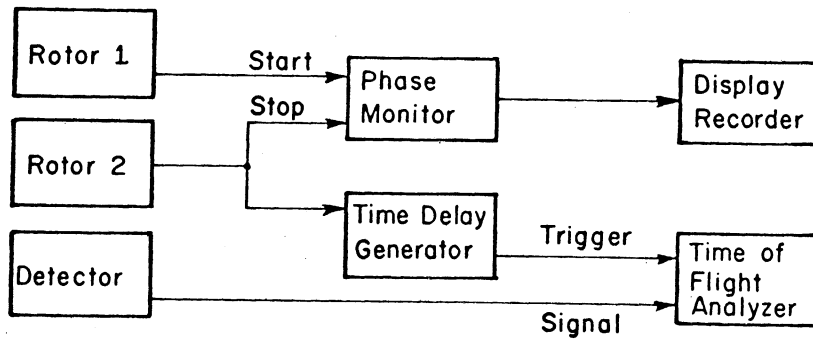


Figure 26. Block diagram showing the routing of signals from various components of the machine during the burst shape measurements.

from this distribution, the faster neutrons would arrive at a downstream detector very soon after the burst was formed, while the slower ones would arrive considerably later. This broadening of the burst would make interpretation of measurements difficult. A single neutron speed was therefore selected by erecting a monochromating crystal (D) in the beam. A thin detector (E) was placed in the deflected beam.

The angle through which the beam was deflected (which is equal to twice the Bragg angle) was established by the following technique. On a calibrated circular scale centered at the middle of the crystal face, a small-diameter $BF_3$ detector was placed at the desired deflection angle. The crystal was rotated until the beam fell in this detector. The crystal was left in this position and the $BF_3$ detector was replaced by the large-area, thin detector, which was assumed to intercept the entire reflected beam.

In order to bring rotors 1 and 2 into the correct phase relation to one another, a timing signal (F) was derived from the shaft of each rotor. These signals occurred at well-known times relative to the times at which the rotors reached their open positions. The time interval between the pulses from the two rotors was measured by a phase monitor (G). The timing pulse from rotor 2 was also used as a time-reference for the counting system. Since it was necessary to introduce a time delay between the occurrence of the pulse from rotor 2 and the beginning of the counting

cycle, the pulse was fed through a time-delay generator (H),
the output pulse from which triggered the time analyzer (I).

The sequence of events is illustrated in figure 27 . Let
us say that the first event is the occurrence of the timing
pulse from rotor 1. This event precedes the opening of rotor
1 by an angle $\theta_1$, through which the rotor, turning at speed
$\omega/4$, moves in time $\dfrac{4\theta_1}{\omega}$. The timing pulse from rotor 2 occurs
at time $t_\varphi$ after that from rotor 1, and rotor 2, turning at
speed $\omega$, opens a time $\dfrac{\theta_2}{\omega}$ later. If $L_{12}$ is the distance
between the centerlines of rotor 1 and rotor 2, and the neu-
tron speed selected by the crystal is v, then these neutrons
travel from rotor 1 to rotor 2 in the time $\dfrac{L_{12}}{v}$ . For the
two-rotor system to pass this speed optimally (more accurately,
to insure that rotor 1 has no part in forming the burst of
neutrons) the phase time $t_\varphi$ must be such that

$$\frac{4\theta_1}{\omega} + \frac{L_{12}}{v} = t_\varphi + \frac{\theta_2}{\omega}$$

$$t_\varphi = \frac{4\theta_1 - \theta_2}{\omega} + \frac{L_{12}}{v} \qquad\qquad \text{(VI-1)}$$

In each case the phase time $t_\varphi$ was adjusted to satisfy
equation (VI-1).

Neutrons which cross rotor 2 centerplane when the rotor
is in its full open position (neutrons in the peak of the
burst) travel the distance $L_{2D}$ to the detector in time $\dfrac{L_{2D}}{v}$.
The time analyzer is triggered (that is, its analyzing cycle
is initiated) by a pulse from the delay generator, which
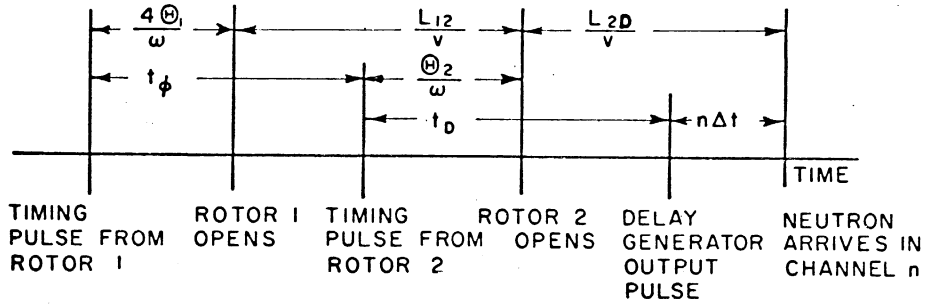pulse follows the timing pulse from rotor 2 after a delay

Figure 27. Time scale of events during one cycle of the machine during the burst shape measurements.
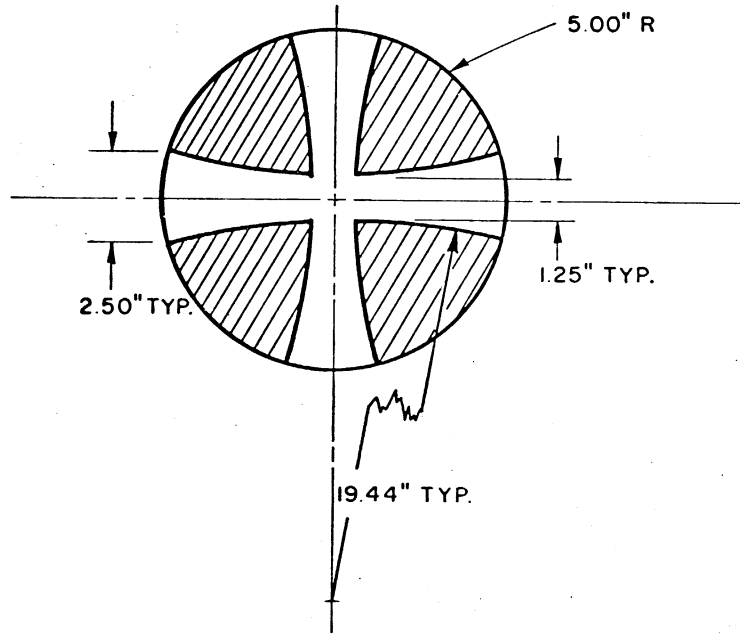


Figure 28. The physical configuration of the fast-neutron rotor. The rotor is constructed of fiberglass-resin laminate.

of length $t_D$. A pulse from the detector which arrives at time $n\Delta t$ after the analyzer is triggered, is stored in channel n of the analyzer. Here, $\Delta t$ is the width of the analyzer time channel, and n is the channel number. In each case the delay time $t_D$ was adjusted so as to cause the neutrons at the peak of burst to be counted at, or near the middle channel of the time analyzer, n = 128. That is, again referring to figure 27, in each case $t_D$ was adjusted so that

$$t_D - \frac{\theta_2}{\omega} + n\Delta t = \frac{L_{2D}}{v} , \quad n \approx 128 \qquad (VI-2)$$

We now undertake to describe the function of each of the significant parts of the device.

## A. Collimator

The collimator resolution-plane geometry is what is important for the present purposes. Shown in figure 25 is the collimation system, in which the collimator is represented as designed. This representation of the collimator is not adequate to predict the burst shapes measured in the experiments discussed here, as was found in the initial comparison of theoretical and experimental results. Development of a more adequate representation is discussed below.

## B. Rotor 1

This rotor is of fiberglass-resin laminate, with slit configuration as detailed in figure 28. The rotor has two

identical, symmetric slits, oriented at $90^{\circ}$ with respect to one another. It therefore produces four bursts per revolution and is turned at one-fourth the speed of the chopping rotor. Its purpose in this experiment was to reduce the background due to epicadmium neutrons.

C. Rotor 2

This rotor is of high-strength Mg-Zn alloy containing 10% Cd for neutron attenuation, and although practically opaque to thermal neutrons, it is quite transparent to neutrons above the cadmium cutoff. Its slit configuration is as shown in figure 29; one burst is produced per revolution. Description of the mechanism of burst formation by this rotor is the primary object of this paper, and has been thoroughly discussed above. It remains to be said of this analysis however, that in the interest of simplicity the three slits in the rotor have been treated as central slits. That is, the formulae derived above have been developed for a slit rotating about a point at its center, and these formulae have been applied in the analysis to all three slits. The approximation involved is of the order of that made in setting $\cos \frac{h}{R} = 1$ where $\frac{h}{R} = .05$.

Surfaces of the slits are circular arcs concentric with the arc of the central slit centerline.

The design ratio of neutron speed to peripheral velocity is $\frac{v_{opt}}{R \, \omega} = 8$ , which leads to the choice of the radius of curvature of the central slit centerline. The arc,

VIEW A
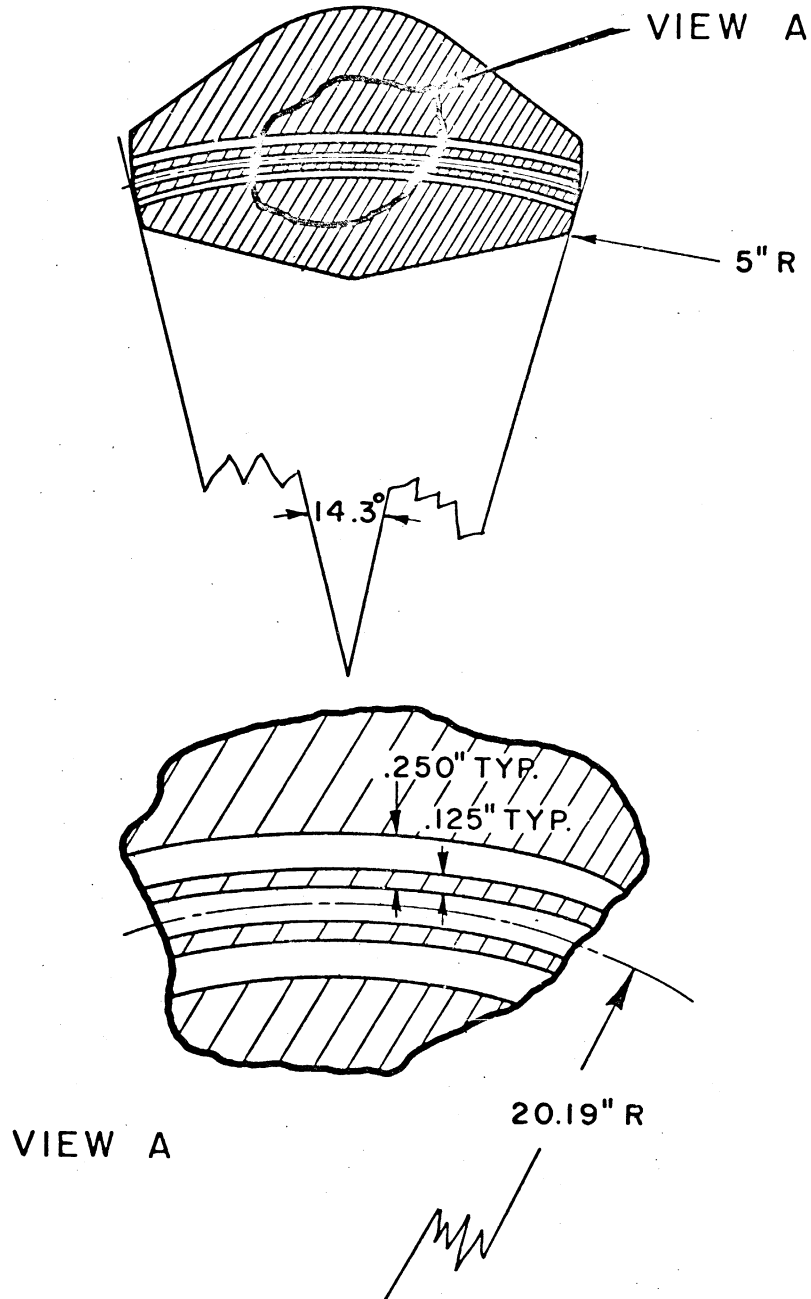
5" R

14.3°

.250" TYP.

.125" TYP.

20.19" R

VIEW A

Figure 29. The physical configuration of the thermal neutron rotor. The rotor is of Mg-Zn-Cd alloy.

$\varphi = 14.3^\circ$ is an alternative parameter indicating the optimum neutron speed, $v_{opt} = \frac{2R\omega}{\varphi}$ . Thus to apply the results of Chapter III, the correspondence principle, to the formulae of Chapters II, IV and V, it is necessary to replace $\frac{1}{v}$ appearing there by $\frac{1}{v} - \frac{1}{v_{opt}} = \frac{1}{v} - \frac{\varphi}{2R\omega}$ .

## D. Crystal Spectrometer

The operation of the crystal spectrometer used to select a well-defined energy from the chopped beam has been discussed above, but the details of the device are as follows. The monochromator was a crystal of Copper, cut on the (200) plane. Spacing for this plane is 1.816 Å. Mosaic width of this crystal has been measured[7] to be 4 minutes of arc, and the contribution to the experimental resolution width is correspondingly small. Since

$$\frac{\Delta t}{t} = \frac{\Delta \lambda}{\lambda} = \cot \theta_B \, \Delta \theta \, , \, \Delta \theta = 4' = .0012 \text{ rad.}$$

and flight times do not exceed 1000 microseconds, this contribution to the resolution is approximately 2.0 microsecond and is neglected.

## E. Detector

The detector used for measurements of the burst shapes was one of the type described in reference 8.* The detector thickness contributes to the resolution of the experiment to a negligible extent, since $\frac{\Delta t}{t} = \frac{\Delta L}{L}$

---

(7)   J. L. Donovan, private communication
*See (8) on next page

where $\Delta L$ is the thickness of the detector, $\simeq .3$ cm, while $L_{2D}$ is

the flight path of neutrons from rotor to detector, approxi-

mately 1.5 meters. Thus

$$\frac{\Delta t}{t} = \frac{.3}{150} = .002$$

and the time uncertainty thus introduced for flight times of

about 1000 microseconds is 2 microseconds, at maximum. This

effect in the measured function is also neglected.

F. Shaft Angle and Frequency Signal Source

This device consists of two parts; a disc which is

attached to the top of the shaft driving the rotor, and a

magnetic pickup mounted in a fixed position perpendicular to

the rotating disc. The disc is of aluminum and contains a

1/32" wide slug of iron in its periphery. The pickup is a

high-output permanent magnet pickup (Electro-Mation Model

3030 AN). As the iron slug passes the pickup, a timing

pulse is produced which appears as in figure 30.



200 to 400
VOLTS

$t$
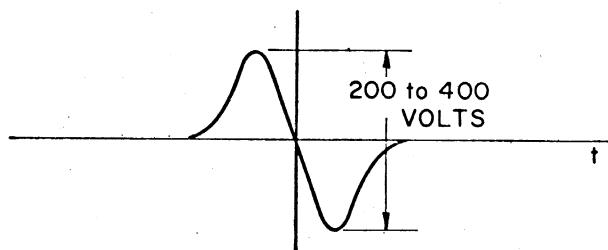
Figure 30. Shape of the timing pulse from the magnetic
pickup.

(8) Vincent, D.H.; Carpenter, J.M.; and Sutton, J.D.;
"A Thermal Neutron Detector Using LiF and Scintillating
Plastic," Bulletin of the American Physical Society, series
II, Vol. 8, No. 4, (1963), Paper UA-12.

For this series of measurements, the lag angles $\theta_1$ and $\theta_2$ (see figure 27) were $\theta_1 = 135^\circ$ and $\theta_2 = 62^\circ$

G. Phase Monitor

The phase monitor is an electronic device which measures the time interval between the occurrence of two events, in this case the occurrence of a pulse from rotor 1 and 2. Refer to figure 31.



Figure 31. Block diagram of the phase monitor circuit.

This description omits some of the workings of the circuit but serves to indicate its general manner of operation.

A pulse from rotor 1 closes a circuit so that pulses from a 1-Mc clock are counted on a scaler. The scaler counts until a pulse from rotor 2 opens the circuit, thus stopping the scaler in which are registered a number of counts proportional to the time interval between pulses from rotor 1 and 2. The output is read out in two ways: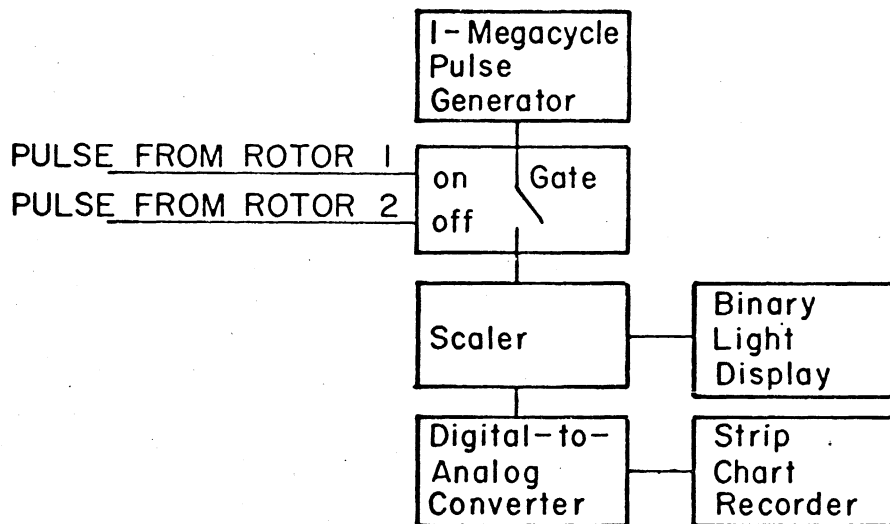 on a binary light display and, through a digital-to-analog converter (which produces a d.c. voltage proportional to the number in the scaler) to a stripchart recorder which continuously monitors changes in the phase time.

This device, the phase monitor, is a crucial part of the system inasmuch as the data it provides are used to set and maintain the correct phasing between rotors.

## H. Time-Delay Generator

One of the functions of the Tektronix Model 535-A oscilloscope is to produce an output pulse at a set time after a triggering pulse is received. The pulse from rotor 2 was used as trigger and the output pulse from the oscilloscope was delayed by whatever time was required to place the burst of neutrons near the center of the time interval scanned by the time-of-flight analyzer, chosen according to formula VI-2.

## I. Time Analyzer

The time analyzer used was a TMC Model CN-110 computer with Model 211 time-of-flight input. Its function is to store signal pulses in memory channels according to the time

at which the signal pulses arrive, relative to the time at
which a triggering pulse arrives. The time interval associated
with each memory channel can be varied in steps from .25 to
64 $\mu$sec., and a time of 16 $\mu$sec. is required to perform the
storage operation. That is, the dead time of the instrument
is 16 microseconds.

Delayed pulses from the oscilloscope were used to
trigger the analyzer, and pulses from the detector were used
as input. For all runs, the channel width was 1 $\mu$sec.

Using the equipment as described, burst shape data were
accumulated for five different neutron speeds (crystal
angles) and five different rotor speeds for each neutron
speed. The results of several of these runs are presented
below, and compared with the theoretical predictions.

COMPARISON OF EXPERIMENTAL AND THEORETICAL RESULTS

The difficulty with regard to the collimator was men-
tioned above in Section VI-A. Comparison of burst shapes
predicted under the assumption that the collimator was as
designed, with measurements, showed poor agreement. To
provide a modified representation of the collimator, data
from an experiment originally performed to locate the
collimated beam, were analyzed for this purpose. This mea-
surement was made in the following manner. At two posi-
tions downstream from the collimator, a strip of gold foil
was placed perpendicularly across the beam in the resolu-
tion plane, and activated by neutrons streaming from the
reactor through the collimator. The foil strips were
scanned by a small-aperture detector to determine the acti-
vation per unit length as a function of position in the beam.
This activation at each point is proportional to the neutron
flux at that point.

This flux may be predicted using the methods of
reference $\because$ and is proportional to an integral

$$N(x,z) = \int P_C(x,z,\psi) \, d\psi$$

over the P-gram which may be interpreted as the $\psi$-interval
containing allowed trajectories at a point x, z. Figure
32 shows the measured activation density, and the predicted
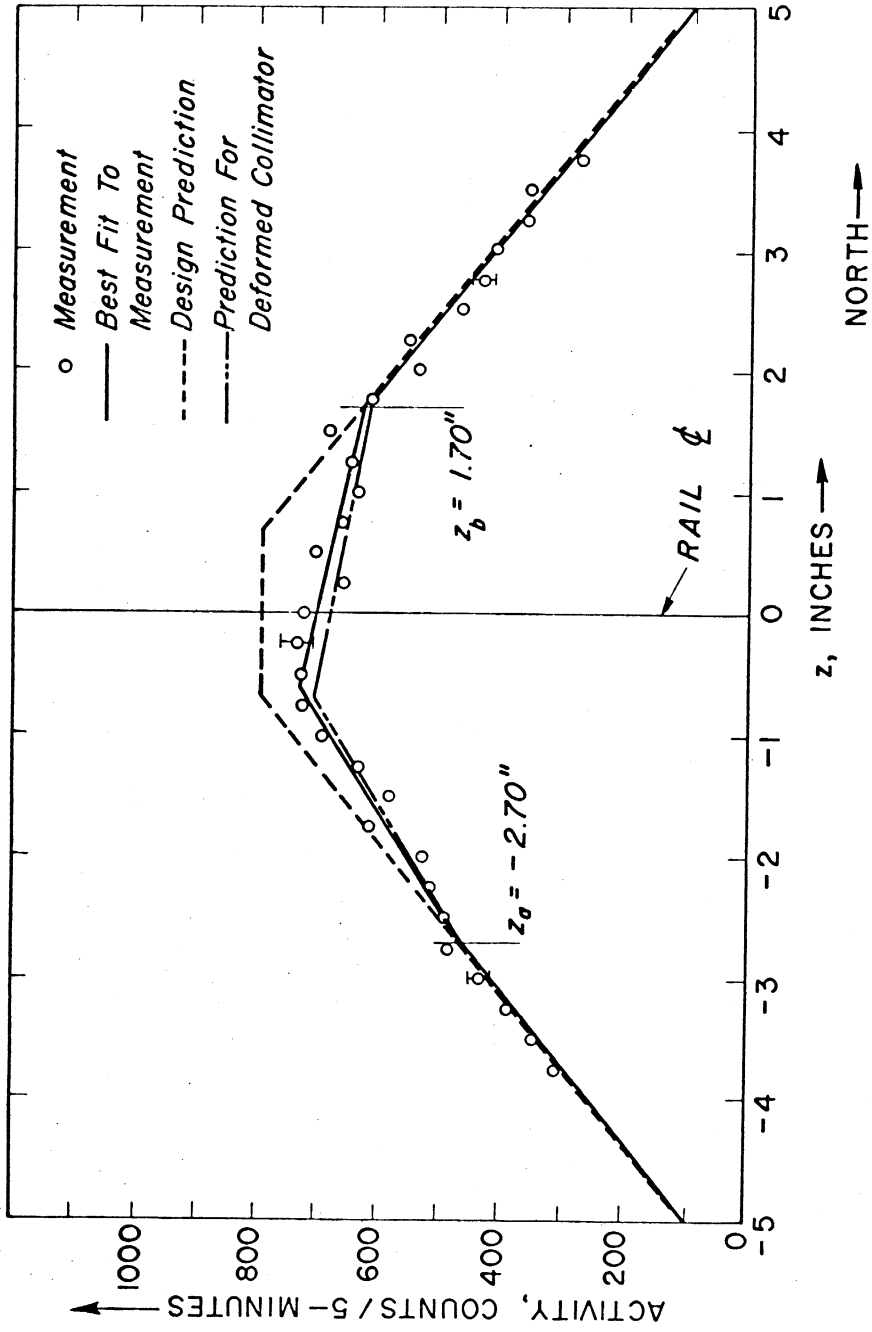density assuming the collimator to be as designed (the

Figure 32. Horizontal foil strip activity at a position
132" from the collimator exit.

design prediction) for a position 132" from the collimator
exit. The measured activation density deviates from the
design prediction in a manner which suggests that the colli-
mator wall is not flat, as shown in figure 25, but rather
contains a lump or bulge, which can be represented approxi-
mately as an edge, as in figure 33.
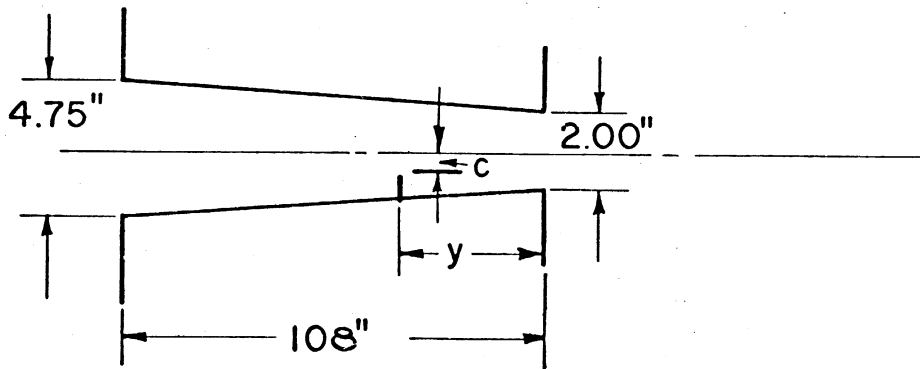


Figure 33. Assumed form of the deformation of the collimator.

The position and height (two parameters) of the bulge
were determined so as to fit the points $z_a$ and $z_b$ at which
the measured activation begins to deviate from the design
prediction. The activation predicted using this model of
the deformed collimator is also shown in figure 32. The
analysis produced a value for the position of the bulge,
y = 15" from the collimator exit, on the south collimator
wall, and a value for the height of the bulge, c = .79"
as shown in figure 33.

Presented as figure 34 is the result of a similar mea-

- 73 -



Figure 34. Horizontal foil strip activity at a position 66" from the collimator exit.

surement at a position 66" from the collimator exit. Also
shown is the prediction using the parameters of the deformed
collimator, assuming the centerline of the rotor support
rails to correspond to that of the collimator. It seems a
better assumption to say that the beam centerline does not
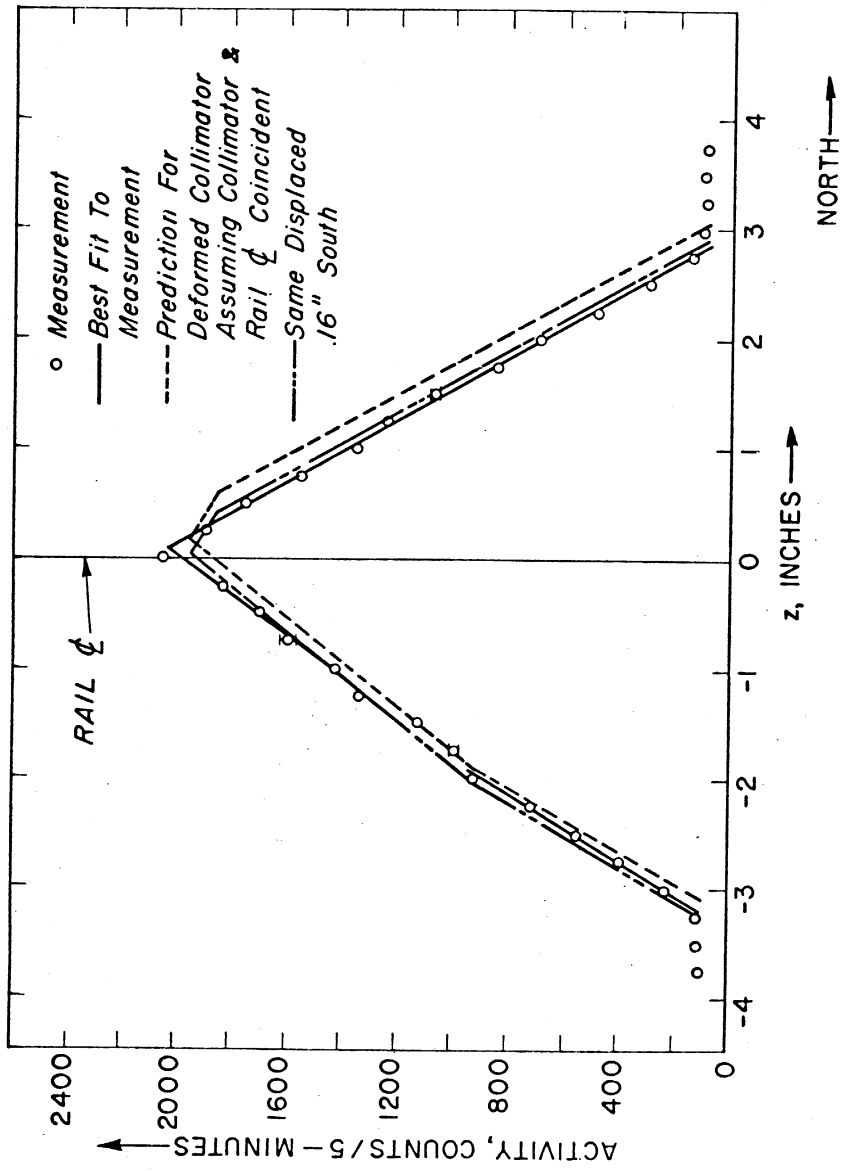coincide with the rail centerline, but instead lies .16"
south. The predicted activation for the deformed collimator,
displaced .16" is also shown in figure 34.

Although the prediction thus generated for the activa-
tion at the 66" position does not match the measurement
exceptionally well, it is an improvement over the design
prediction. Deviations are attributed to the fact that such
a simple model of the deformation is not completely realistic.

Conclusions drawn from this analysis may be summarized.
The collimator is deformed and the deformation may be repre-
sented as in figure 33. The rotor support rails are not
perfectly aligned with the collimator beam centerline, rather
the beam centerline passes the 66" position .16" south of the
rail centerline and passes the 132" position at the rail
centerline. Therefore, we conclude that the collimator is
misaligned by an angle of $\frac{.16"}{66"}$ = .00243 rad., and that
the collimator exit is misplaced a distance (.00243)(132") =
.32", south of the rail centerline.

With this modified representation for the collimator,
a P-gram for the deformed collimator can be constructed, at
the position of the rotor 2 centerplane. This is shown in
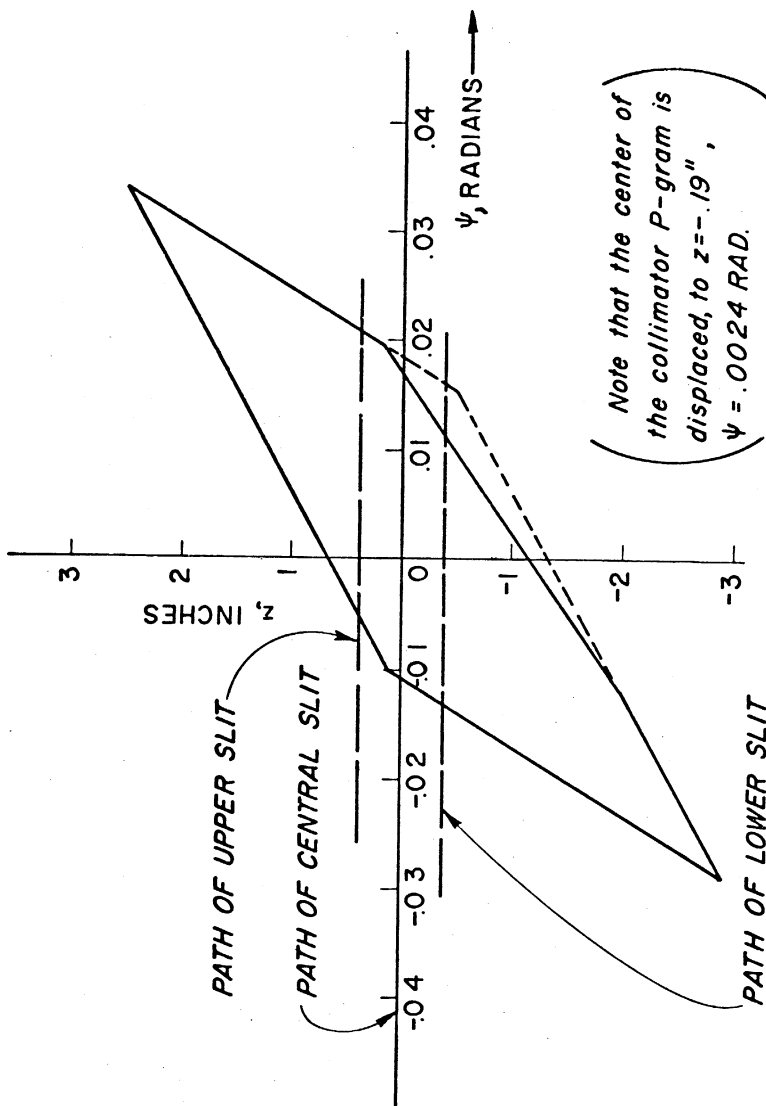figure 35, in which the origin of the z-coordinate is taken

Figure 35. The collimator P-gram at the position of rotor 2 centerplane, 54" from the collimator exit. Drawn for z = 0, $\psi = 0$ on the rotor support rail centerline.

as the position of the rail centerline, while that of the
$\psi$-coordinate is taken as the direction of the rail centerline.
Therefore the collimator P-gram must be drawn displaced, its
center at

$$z = -.32" + 54" \ (.00243)$$

$$= -.32" + .13" = -.19"$$

$$\psi = .00243 \text{ radians}$$

Also shown as figure 35 are the boundaries of the colli-
mator as designed, illustrating the effect of the bulge in
deforming the collimator P-gram. The paths of the P-grams
for the three slits of rotor 2 are also shown on figure 35.
The intersections of these paths with the collimator P-gram
boundaries determine the angles $\psi_{in}$ and $\psi_{out}$ which enter
the arguments of $\Delta Z$.

Recall the result of Chapter IV

$$M(\theta_B, t) = \frac{1}{\alpha} \int P_C(x, z, \xi/\alpha) \ P_R(x, z, \xi - \omega t) d \xi \ d \ z \quad \text{(IV-22)}$$

where $\alpha = (1 + \omega \tau_B \cot \theta_B)$, and for our purposes we may
regard $1/\alpha$ as a constant of normalization.

Also recall the function $\Delta Z(\rho, \eta)$ in terms of which the
calculation of $M(\theta_B, t)$ was cast;

$$M(\theta_B, t) = \Delta Z( \rho_{out}, \alpha \psi_{out} - \omega t) - \Delta Z( \rho_{in}, \alpha \psi_{in} - \omega t)$$

for each slit in the moving rotor; where $\rho$'s and $\psi$'s are
to be chosen for the distended P-gram, i.e., $P_C(x, z, \xi/\alpha)=1$.
The observed burst shape function is the sum of the bursts

from each slit.

From figure 35 the intersection $\psi_{in \atop out}$ and slopes $z/S_{in \atop out}$ are tabulated below in Table 1.

Table VII-1

| | $\psi_{in}$ | $z/S_{in}$ | $\psi_{out}$ | $z/S_{out}$ |
|---|---|---|---|---|
| Upper Slit | -.0053 | 5/54 | .0208 | 5/172 |
| Central Slit | -.0109 | 5/172 | .0169 | 5/69 |
| Lower Slit | -.0133 | 5/172 | .0114 | 5/69 |

Several records have been chosen for comparison with theory: Figure 36 and Table 2 are for rotor speed 440 revolutions/sec. counterclockwise, and $\theta_B$ = 24.5°. ($v_B$ = 2650 $\frac{meters}{sec.}$), (referred to hereafter as record 440-1). Figure 37 and Table 3 are for rotor speed 280 revolutions/sec., counterclockwise and $\theta_B$ = 38.3° ($v_B$ = 1780 M/sec.). (Referred to hereafter as record 280-5).
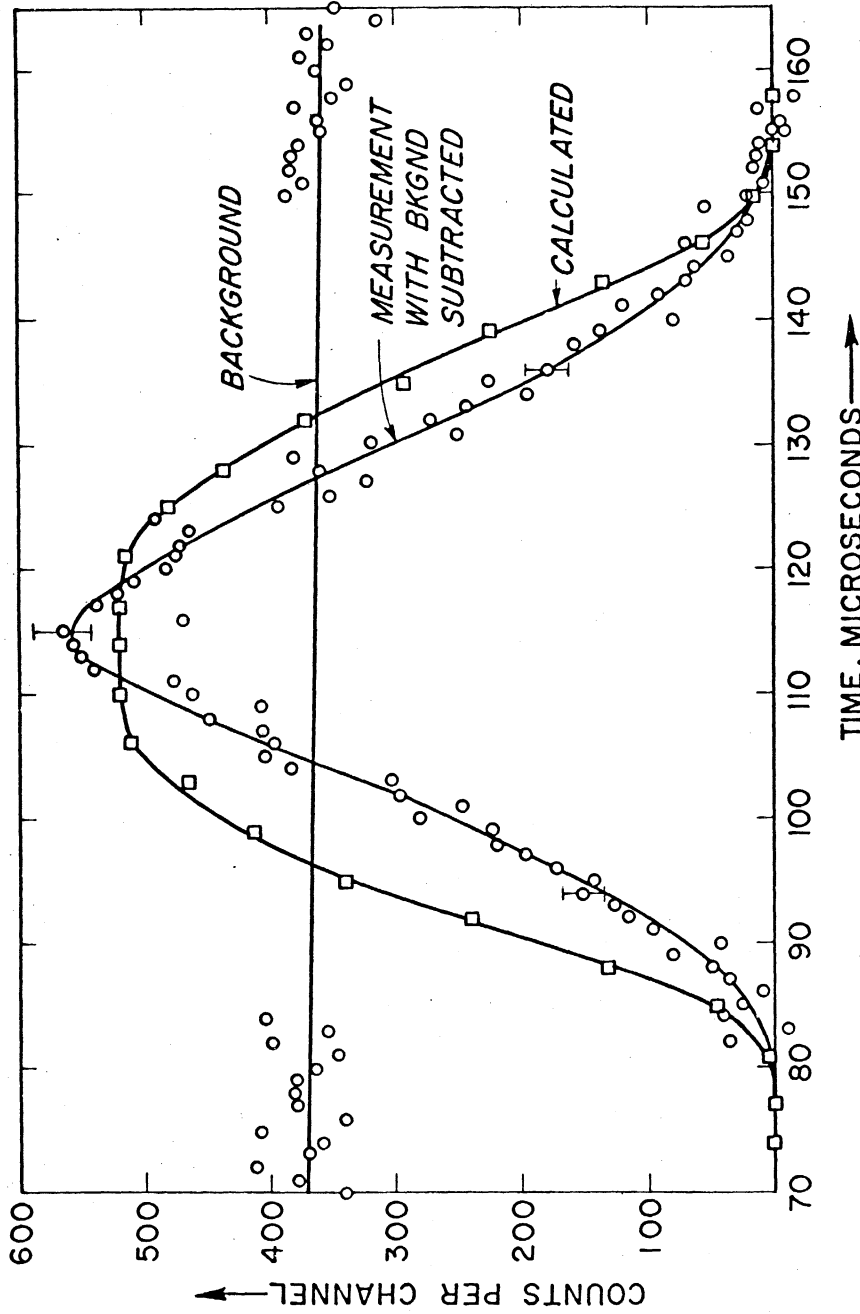
Figure 36. The measured burst shape for rotor angular speed
$\omega$ = 440 cycles per second counterclockwise, and neutron speed
$v_B$ = 2650 meters per second.

Table VII-2

(For Record 440-1)

$\omega$ = 440 cps = 2760 radians/sec. Counterclockwise

$\theta_B = 24.5°$;

$$\lambda_B = 2d \sin \theta_B = 2(1.816) \sin 24.5° = 1.51 \ Å$$

$$v_B = \frac{4000}{\lambda_B} = 2650 \ m/sec$$

$$\cot \theta_B = 2.194$$

$$\tau_B = \frac{L_{2D}}{v_B} = \frac{1.58}{2650} = 5.97 \times 10^{-4} \ sec.$$

$$1 + \omega\tau_B \cot \theta_B = 1 + (5.97 \times 10^{-4})(2.760 \times 10^3)(2.194)$$

$$= 1 + 3.60 = 4.6$$

$$\beta = \frac{R^2\omega}{h}(\frac{1}{v_B} - \frac{1}{v_{opt}}) = \frac{R^2\omega}{hv_B} - \frac{R\varphi}{2h}$$

$$= \frac{(25)(2.54)(2.76 \times 10^3)}{(.25)(2650)} - \frac{(5)(.25)}{2(.25)} = 2.64 - 2.50$$

$$\beta = .14$$

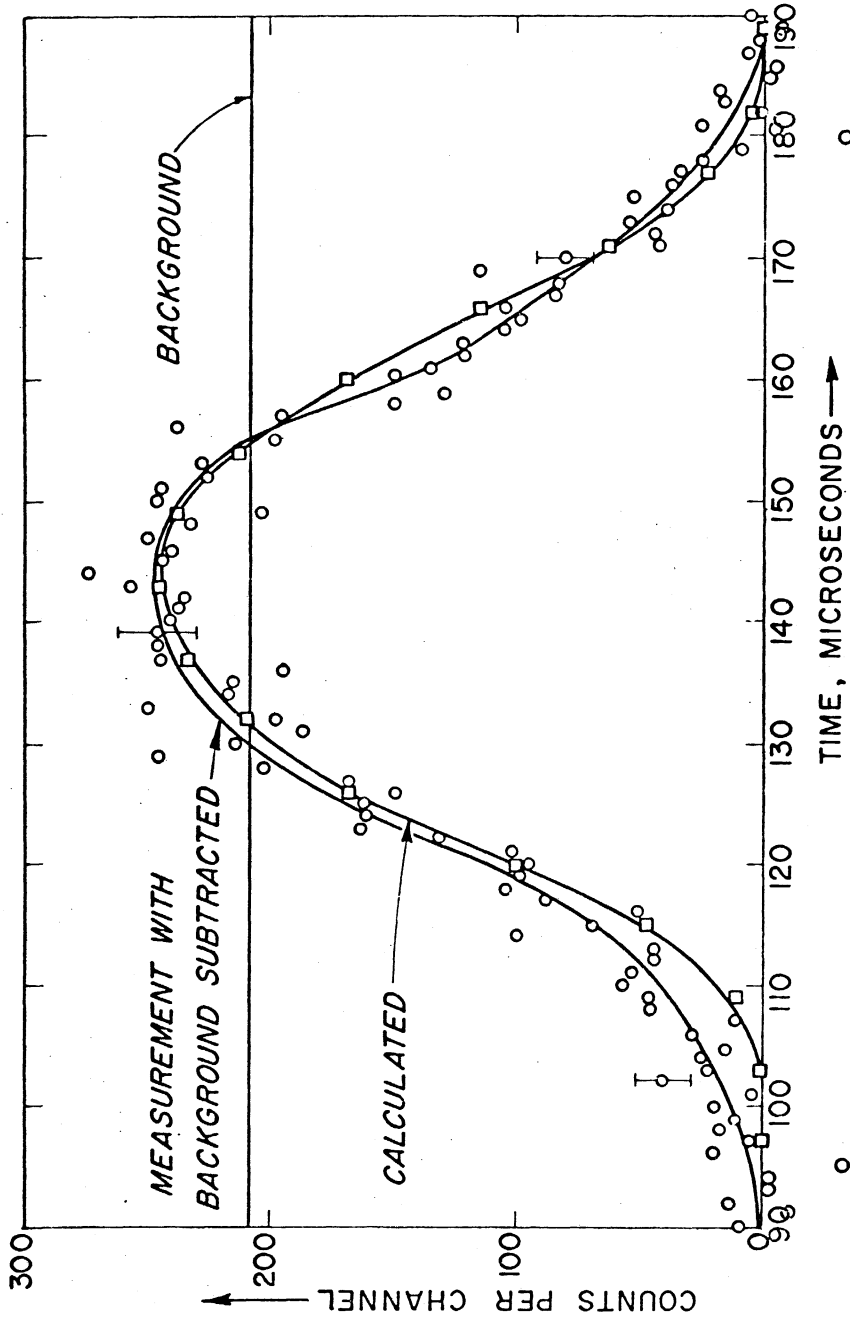| | $\alpha\psi_{in}$ | $\rho_{in}$ | $\alpha\psi_{out}$ | $\rho_{out}$ |
|---|---|---|---|---|
| Upper Slit | -.0243 | .43 | .0956 | .13 |
| Central Slit | -.0501 | .13 | .0778 | .33 |
| Lower Slit | -.0611 | .13 | .0524 | .33 |

Figure 37. The measured burst shape for rotor angular speed
$\omega$ - 280 cycles per second counterclockwise and neutron speed
$v_B$ = 1780 meters per second.

Table VII-3

(For Record 280-5)

$\omega = 280$ cps $= 1760$ radian/sec. Counterclockwise

$\theta_B = 38.3^\circ$

$$\lambda_B = 2(1.816) \sin 38.3^\circ$$
$$= 2.25 \text{ Å}$$

$$v_B = \frac{4000}{\lambda_B} = 1780 \text{ m/sec.}$$

$\cot \theta_B = 1.265$

$$\tau_B = \frac{L_{2D}}{v_B} = \frac{1.58}{1780} = 8.88 \times 10^{-4} \text{ sec.}$$

$$(1 + \omega\tau_B \cot \theta_B) = 1 + (1760)(8.88 \times 10^{-4})(1.265)$$
$$= 1 + 1.98$$
$$= 2.98$$

$$\beta = \frac{R^2 \omega}{h v_B} - \frac{R\Phi}{2h} = \frac{4450}{1780} - 2.50$$
$$= 0$$

|  | $\alpha\psi_{in}$ | $\rho_{in}$ | $\alpha\psi_{out}$ | $\rho_{out}$ |
|---|---|---|---|---|
| Upper Slit | -.0158 | .276 | .0622 | .0869 |
| Central Slit | -.0325 | .0869 | .0505 | .216 |
| Lower Slit | -.0397 | .0869 | .0341 | .216 |

Measurements were also made with the rotors turning

clockwise, i.e., for $\omega$ negative. The effect is to leave all

else unchanged except the factor $1 + \omega\tau_B \cot \theta_B$, in which

the second term, positive for counterclockwise rotation,

becomes negative. With proper choice of parameters, this

factor approaches zero, and the effective width of the colli-

mator angular distribution is zero. What actually happens is

that the collimator angular spread is exactly compensated by

the spread in flight times of neutrons reflected by the

crystal. Under such circumstances, the beam might be said

to be "time focused", and the burst shape seen is that pre-

dicted for a unidirectional, monochromatic beam.

Since it was not possible to reach the condition of time

focusing because of experimental limitations several measure-

ments were made, for varying flight paths from rotor center-

line to detector. In table 4 are exhibited the conditions

for each measurement. Results of these measurements are

shown in figures 38, 39, 40, 41. Plotted on each figure is

the predicted burst shape for the "focussed" condition. In

each case, the prediction is the same function, normalized

to have its area equal to that beneath the measured peak.

Agreement is not expected for any figure, rather it is to be

noted that as the length $L_{2D}$ approaches that "focussed" value,

.80 meters, the measured burst shapes approach the prediction

for the "focussed" condition.

Measurements were also made with the rotors turning clockwise, i.e., for $\omega$ negative. The effect is to leave all else unchanged except the factor $1 + \omega\tau_B \cot \theta_B$, in which the second term, positive for counterclockwise rotation, becomes negative. With proper choice of parameters, this factor approaches zero, and the effective width of the collimator angular distribution is zero. What actually happens is that the collimator angular spread is exactly compensated by the spread in flight times of neutrons reflected by the crystal. Under such circumstances, the beam might be said to be "time focused", and the burst shape seen is that predicted for a unidirectional, monochromatic beam.

Since it was not possible to reach the condition of time focusing because of experimental limitations several measurements were made, for varying flight paths from rotor centerline to detector. In table 4 are exhibited the conditions for each measurement. Results of these measurements are shown in figures 38, 39, 40, 41. Plotted on each figure is the predicted burst shape for the "focussed" condition. In each case, the prediction is the same function, normalized to have its area equal to that beneath the measured peak. Agreement is not expected for any figure, rather it is to be noted that as the length $L_{2D}$ approaches that "focussed" value, .80 meters, the measured burst shapes approach the prediction for the "focussed" condition.

## Table VII-4

Conditions for measurements using clockwise rotation.

For all runs:

$$\omega = 280 \text{ cps. clockwise}$$

$$= 1760 \text{ rad/sec. clockwise}$$

$$\theta_B = 38.3^{\circ}$$

$$\lambda_B = 2.25 \text{ Å}$$

$$v_B = 1780$$

$$\cot \theta_B = 1.265$$

$$1 + \omega\tau_B \cot \theta_B = 1 + \frac{\omega L}{v_B} \cot \theta_B$$

$$= 1 - \frac{1760 \ (1.265)}{1780} L$$

$$= 1 - 1.250 \ L$$

$$\beta = \frac{R^2\omega}{hv_B} - \frac{R\varphi}{2h} = 0$$

For figure 30    $L_{2D} = 1.51$ meters    $1 - 1.25 \ L_{2D} = -.83$

For figure 31    $L_{2D} = 1.45$ meters    $1 - 1.25 \ L_{2D} = -.82$

For figure 32    $L_{2D} = 1.27$ meters    $1 - 1.25 \ L_{2D} = -.58$

For figure 33    $L_{2D} = 1.07$ meters    $1 - 1.25 \ L_{2D} = -.34$

At "focus", $1 - 1.25 \ L_{2D} = 0 \ (L_{2D} = .80$ meters)

Figure 38. The measured burst shape for rotor angular speed $\omega$ = 280 cycles per second clockwise and neutron speed $v_B$ = 1780 meters per second, with the detector 1.51 meters from the rotor centerplane.

Figure 39. The measured burst shape for rotor angular speed
$\omega = 280$ cycles per second clockwise and neutron speed
$v_B = 1780$ meters per second, with the detector 1.45 meters
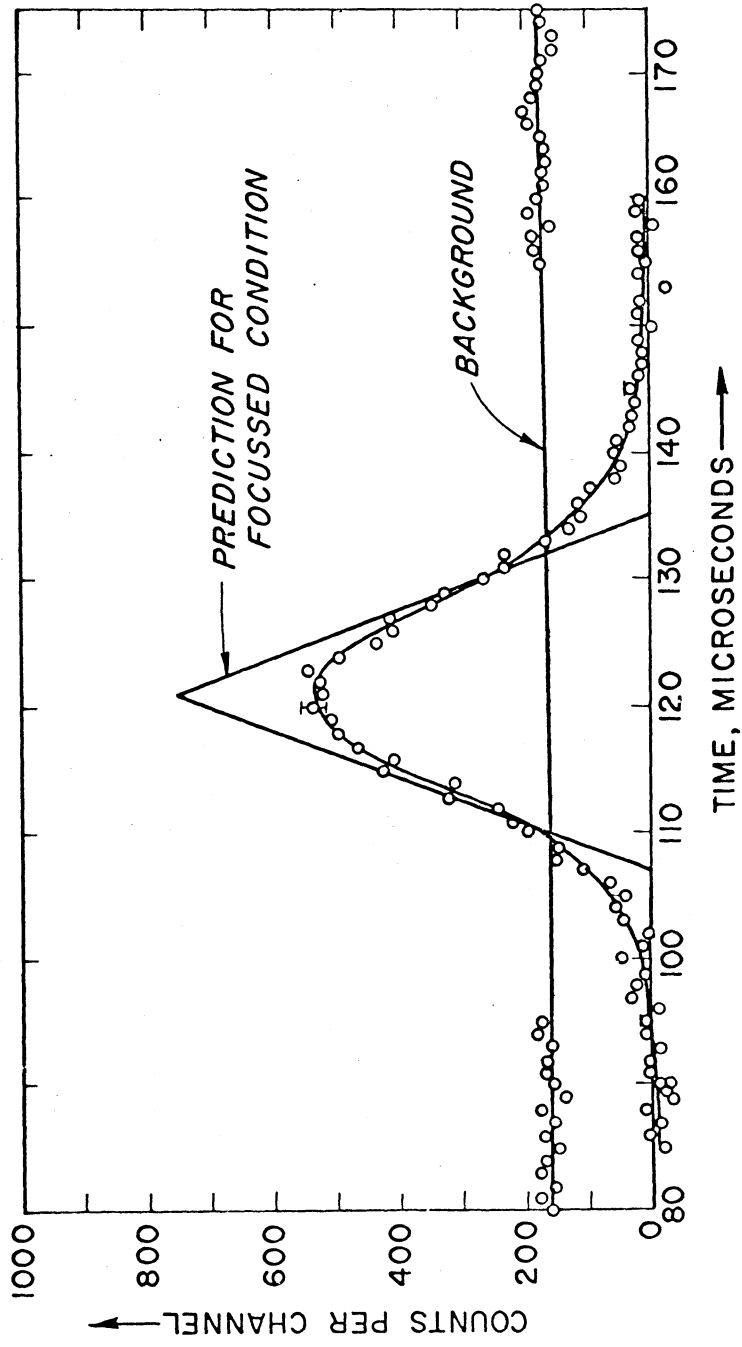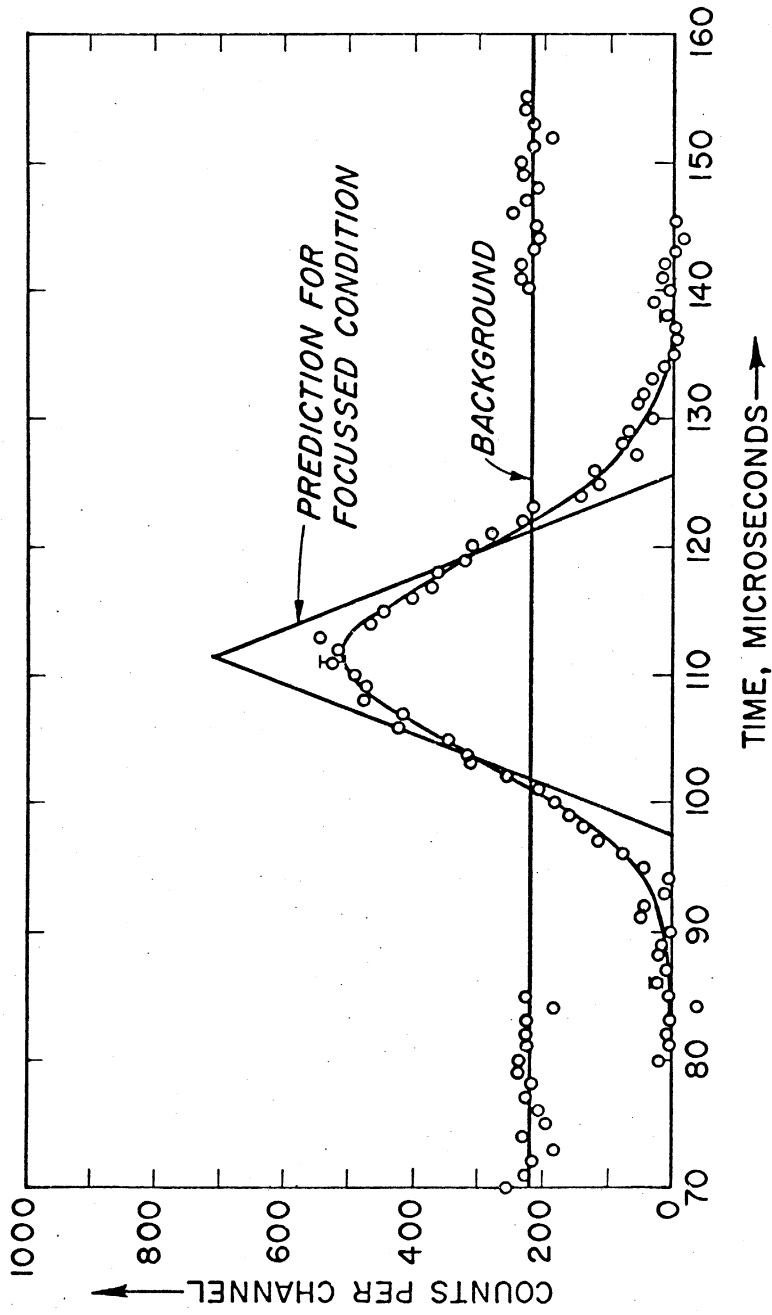from the rotor centerplane.

Figure 40. The measured burst shape for rotor angular speed
$\omega$ = 280 cycles per second clockwise and neutron speed
$v_B$ = 1780 meters per second, with the detector 1.27 meters
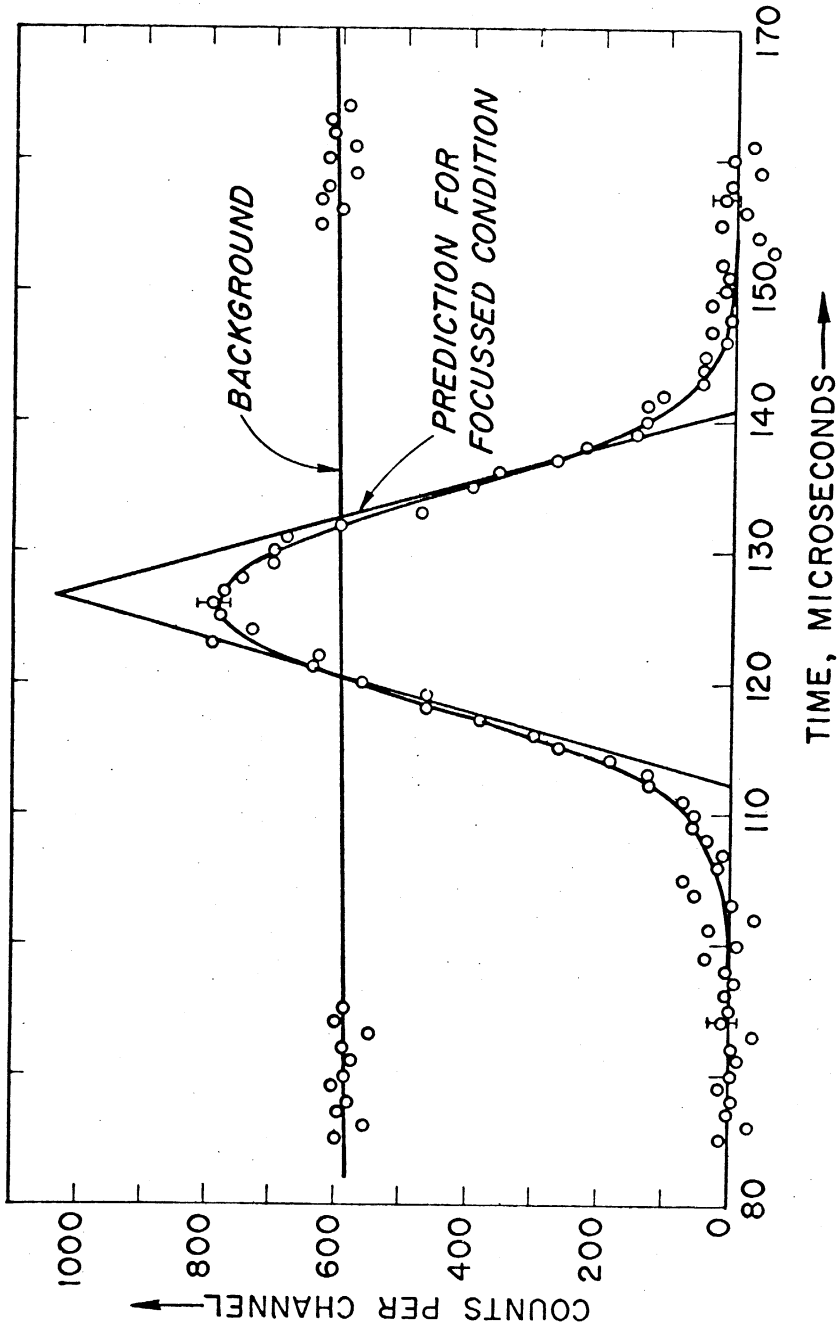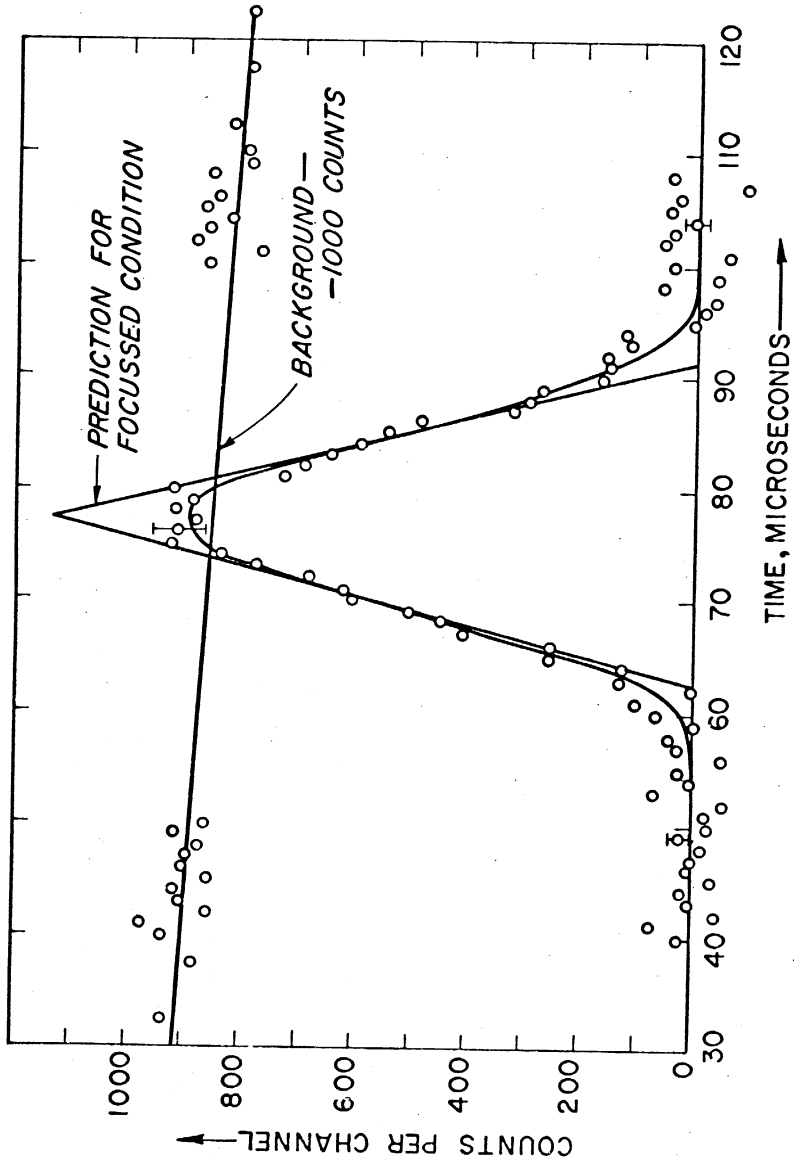from the rotor centerplane.

Figure 41. The measured burst shape for rotor angular speed
ω = 280 cycles per second clockwise and neutron speed
$v_B$ = 1780 meters per second, with the detector 1.07 meters
from the rotor centerplane.

# CHAPTER VIII

## DISCUSSION AND CONCLUSION

Comparisons of experimental data with predictions from the theory developed above were displayed in the preceding chapter for several situations. With regard to the justification of the theory by comparison with these data, let it first be said that the experiments were designed for another purpose. Therefore, some difficulties are to be anticipated, due to the fact that certain conditions were not well established and certain parameters necessary to the analysis, were not well measured. This was true with respect to one most important length, $L_{2D}$ from the rotor centerplane to the detector. This length establishes not only the magnitude of the factor $(1 + \omega\tau \cot \theta)$, but also the location of the chopping rotor. The length $L_{2D}$ was inferred from measurements of times of flight. A large number of burst shapes were measured, of which those presented are only representative. For each measurement, the neutron velocity was well known as well as time of arrival relative to the time at which the chopping rotor opened (i.e. the flight time.) The length $L_{2D}$ used here is the average value of the product of the neutron velocity and the flight time, from a large number of measurements. It is also true that the knowledge of the shape of the collimator P-gram is not exact, as was already discussed.

Further there is the lingering doubt as to the chopping

effect of rotor 1, (which was assumed to have no effect on the chopped beam.) This effect can be computed by the method of this paper, but the approach undertaken here has been to present formulae and methods adaptable to hand calculation. As a practical matter this almost precludes even undertaking to estimate this effect, or to judge the conditions under which it is present or absent, within a reasonable time.

With these apologies, the relatively poor agreement between prediction and measurement shown for figure 36, may not be surprising. This is so because in that case, the effect of the collimator is exaggerated to its maximum extent (because the factor $(1 + \omega\tau_B \cot \theta_B)$ is largest.), and any errors in the same factor (arising due to error in $L_{2D}$ or inaccuracies in the description of the collimator) are therefore similarly at maximum.

The situation with respect to figure 37 is in contrast to that of figure 36.* Here, agreement between prediction and measurement is highly convincing. This may be somewhat fortuitous, but it is to be noted that in this case, the effects of the doubtful collimator data are smaller than for the measurement of figure 36.

---

*Here one should note that there are two compensating effects establishing the width of the burst shape, which is given by

$$\Delta t = \frac{1}{\omega}(1 + \omega\tau_B\cot \theta_B)\Delta\psi_{collimator} + \Delta\psi_{rotor}$$

$$= \frac{\Delta\psi_{coll.} + \Delta\psi_{rot.}}{\omega} + \tau_B\cot \theta_B \, \Delta\psi_{coll.}$$

The first term is larger in the cases of the lower frequency, while the second term, which varies as cosine $\theta_B$, is smaller for larger Bragg angles, and tends to compensate.

Further substantiation of the theory is exhibited in the sequence of figures 38, 39, 40, 41, for varying lengths $L_{2D}$. In each case the unidirectional-beam prediction is superposed upon the plot of the measured function. To be especially noted is the fact that the measured functions approach this prediction as the length $L_{2D}$ approaches the focussed condition.

In the light of these comparisons, it is concluded that the theory is well substantiated by the measurements. However, the theory itself is intrinsically satisfying, because of the insight it provides into the mechanism of burst formation in a chopping device. This is in addition to, or perhaps the basis for the fact that calculations of the burst formation follow readily from the P-gram theory, as it has been applied.

Reflecting, we can see those points at which significant clarifications and simplifications have come about due to the use of the P-gram theory. The first is the manner in which expressions for the expected counting rates are formulated, as in equations II-21 and IV-19. Here, the expressions involve functions either subject to straightforward measurement (as in the case of the incident neutron intensity), or available from other theory (as in the case of the crystal reflection) or calculable from the P-gram theory. Inasmuch as these formulae give instantaneous counting rates, they can also be used to give long-time-average counting rates, and resolution

functions.

Second is the straightforward explanation the theory provides for the effect of the monochromating crystal in a chopped beam. Third is the ease with which the chopping effects of several rotors in sequence can be understood, by merely considering several rotor transmission probabilities, that is, by superposing several rotor P-grams on the same plane.

A digital computer code could be written applying the P-gram concept to more complex systems. The code might be one which samples points in the trajectory plane ($z - \psi$ plane), and makes decisions whether successive points be within the P-grams for each element of a device. It would be fairly easy to include the effects of semi-transparent (as opposed to totally opaque vs. perfectly transparent) components in such a code.

A further clarification of chopper dynamics is in the theorem of Chapter III, which doubtlessly is not new, and indeed has been proved approximately in reference 3. However, the proof is without approximation here, and is new in this context. The proof as detailed has the advantage that the method for calculating apparent boundary transformations is a part of the proof.

The methods of analysis presented here could be generalized to treat many of the common forms of neutron spectrometers. Indeed these same techniques may possibly also be applied to analysis of systems employing other radiations.

# APPENDIX
## EXPANSION OF THE FUNCTION $z_u(\eta)$ ABOUT $\rho = 0$

In order to avoid the difficulties associated with calculating the values of the functions (V-30) and (V-34) near the removable singularity at $\rho = 0$, we remove the singularity in an expansion in powers of $\rho$. The term on which we focus attention is the radical,

$$(\frac{\delta\rho}{2} + \frac{\beta\delta}{\rho} + \eta)^{3/2} = (\frac{\beta\delta}{\rho})^{3/2} (1 + \frac{\rho\eta}{\beta\delta}(1 + \frac{\rho\delta}{2\eta}))^{3/2}$$

(A-1)

in which the largest term is $\frac{\beta\delta}{\rho}$, the smallest, $\frac{\delta\rho}{2}$. The binomial expansion

$$(1 - x)^P = \sum_{n=0}^{\infty} \frac{(-P)_n}{n!} x^n$$

(A-2)

where

$$(\alpha)_n \equiv (\alpha)(\alpha + 1)(\alpha + 2) \cdots (\alpha + n - 1)$$

(A-3)

$$(\alpha)_0 \equiv 1$$

applied to A-1 gives

$$(\frac{\delta\rho}{2} + \frac{\beta\delta}{\rho} + \eta)^{3/2} = (\frac{\beta\delta}{\rho})^{3/2} \sum_{n=0}^{\infty} \frac{(-3/2)_n}{n!} (-1)^n (\frac{\rho\eta}{\beta\delta})^n (1+\frac{\rho\delta}{2\eta})^n$$

(A-4)

Another application gives

$$(1 + \frac{\rho\delta}{2\eta})^n = \sum_{k=0}^{n} \frac{(-n)_k}{k!} (-1)^k (\frac{\rho\delta}{2\eta})^k$$

(A-5)

so that

$$(\frac{\delta\rho}{2} + \frac{\beta\delta}{\rho} + \eta)^{3/2} = (\frac{\beta\delta}{\rho})^{3/2} \sum_{n=0}^{\infty} \sum_{k=0}^{n} \frac{(-3/2)_n (-n)_k}{n! \; k!} (\frac{\rho\eta}{\beta\delta})^n \times$$

$$\times (\frac{\rho\delta}{2\eta})^k (-1)^{n+k}$$

$$= (\frac{\beta\delta}{\rho})^{3/2} \sum_{n=0}^{\infty} \sum_{k=0}^{n} \frac{(-3/2)_n (-n)_k}{n! \; k!} (\frac{1}{2})^k (\frac{\eta}{\delta})^{n-k} (\frac{1}{\beta})^n \rho^{n+k} (-1)^{n+k}$$

$$(A-6)$$

For $k \geqslant 0$,

$$(-n)_k = (-n)(-n + 1) \cdots (-n + k - 1)$$

$$= (-1)^k \frac{n(n-1) \cdots (n - k + 1)(n - k) \cdots 1}{(n - k)(n - k - 1) \cdots 1}$$

$$= \frac{(-1)^k n!}{(n - k)!}$$

$$(A-7)$$

Thus

$$(\frac{\delta\rho}{2} + \frac{\beta\delta}{\rho} + \eta)^{3/2} = (\frac{\beta\delta}{\rho})^{3/2} \sum_{n=0}^{\infty} \sum_{k=0}^{n} \frac{(-3/2)_n (-1)^k}{k! \; (n - k)!} (\frac{1}{2})^k (\frac{\eta}{\delta})^{n-k} \times$$

$$\times (\frac{1}{\beta})^n \rho^{n+k} (-1)^{n+k}$$

$$(A-8)$$

Replacing n by n - k everywhere leads to the more appropriate

form [9]

$$(\frac{\delta\rho}{2} + \frac{\beta\delta}{\rho} + \eta)^{3/2} = (\frac{\beta\delta}{\rho})^{3/2} \sum_{n=0}^{\infty} \sum_{k=0}^{[n/2]} \frac{(-3/2)_{n-k} (-1)^n}{k! \; (n - 2k)!} \times$$

$$\times (- \frac{1}{2\beta})^k (\frac{\eta}{\beta\delta})^{n-2k} \rho^n$$

$$(A-9)$$

[9] Rainville, E.D.; "Special Functions", The Macmillan
Company, New York (1960) p. 56

The symbol $\left[n/2\right]$ is defined to be the greatest integer in $\frac{n}{2}$, that is, for example, if $\frac{n}{2} = \frac{7}{2}$, $\left[n/2\right] = 3$.

In full, then the function $Z_u(\eta)$ may be represented

$$Z_u(\eta) = R\left\{ \frac{\eta^2}{2\rho} + \frac{2\delta\beta}{\rho^2}\eta - \right.$$

$$- \frac{4}{3}\frac{\beta^2\delta^2}{\rho^3} \sum_{n=3}^{\infty} \sum_{k=0}^{\left[n/2\right]} \frac{(-3/2)_{n-k}(-1)^n}{k!(n-2k)!}(-\frac{1}{2\beta})^k(\frac{\eta}{\beta\delta})^{n-2k}\rho^n -$$

$$\left. - \frac{4}{3}\frac{\beta^2\delta^2}{\rho^3} - \frac{2\delta\beta}{\rho^2}\eta - \frac{\eta^2}{2\rho} - \frac{\beta\delta^2}{\rho} - \frac{\delta^2\rho}{8} + \frac{\beta\delta^2}{\rho} + \frac{4}{3}\frac{\beta^2\delta^2}{\rho^3} \right\}$$

$$(A-10)$$

In this form the negative powers of $\rho$ vanish, and

$$Z_u(\eta) = R\left\{ -\frac{\delta^2\rho}{8} - \frac{4}{3}\frac{\beta^2\delta^2}{\rho^3} \sum_{n=3}^{\infty} \sum_{k=0}^{\left[n/2\right]} \frac{(-3/2)_{n-k}(-1)^n}{k!(n-2k)!} \right. (x)$$

$$(x) (-\frac{1}{2\beta})^k(\frac{\eta}{\beta\delta})^{n-2k}\rho^n$$

$$(A-11)$$

As is suggested by the form of the generating function, the polynomials appearing in the expansion A-11 are a type of ultraspherical polynomial, of which the well-known Legendre polynomials are a special case. This knowledge could be helpful in performing calculations from A-11, except for the fact that these polynomials are not commonly found in tabulated form.

# BIBLIOGRAPHY

REFERENCE

(1)   Fermi, E.; Marshall, J.; and Marshall, L.; Phys. Rev. $\underline{72}$, p. 193 (1947)


(2)   Stone, R.S.; and Slovacek, R.E.; KAPL 1499 (1956)


(3)   Marseguerra, M.; and Pauli, G.; Nuclear Instruments & Methods $\underline{4}$, pp. 140 - 150; (1959)


(4)   Carpenter, J.M.; Work Unpublished


(5)   Bacon, "Neutron Diffraction," p. 64, 82, Oxford University Press, London (1955)


(6)   Egelstaff, P.A.; Cocking, S.J.; and Alexander, T.K.; IAEA Proc. of the Symposium on Inelastic Scattering of Neutrons in Solids & Liquids, Vienna, Oct., 1960, p. 165 IAEA (1961)


(7)   Donovan, J.L.; private communication


(8)   Vincent, D.H.; Carpenter, J.M.; and Sutton, J.D.; Bulletin of the American Physical Society, Series II, Vol. 8, No. 4 (1963) Paper UA-12


(9)   Rainvile, E.D.; "Special Functions," The Macmillan Company, New York (1960) p. 56